CENTRO DE INVESTIGACIONES EN ÓPTICA, A.C.

ALGORITHMS FOR THE DIGITAL PRESERVATION OF THE MORPHOLOGY OF SEMI-FOSSILIZED PIECES THROUGH NON DESTRUCTIVE OPTICAL TECHNIQUES

Dissertation presented in partial fulfillment of the requirements for the degree of Doctor in Science (Optics)

Presented by: M.Sc. Juan Carlos Gutiérrez García
Advisor: Dr. Amalia Martínez García

Versión definitiva. Incluye cambios sugeridos por revisores.

_____
Vo. Bo. Amalia Martínez García

November 2015
León, Guanajuato, México

This work is dedicated to my beloved family…

Acknowledgements

I would like to thank all the persons that supported me in some way to get my doctoral degree.

To my advisors, Dr. Amalia Martínez García and Dr. Juan F. Mosiño, for their guidance and patience during this period, for the knowledge and experience shared that helped me to be former as a researcher. To my evaluation committee Dr. Joaquín Arrollo Cabrales, Dr. Iván Toto Arellano, Dr. Manuel de la Torre Ibarra, and Dr. Mauricio Flores Moreno for their valuable comments which allow me to improve this thesis.

I wish to thank deeply the support of the Center for Research in Optics (Centro de Investigaciones en Óptica, CIO) and the Mexican National Science and Technology Council (Consejo Nacional de Ciencia y Tecnología, CONACYT) through scholarship grant 207796 as well as through grant 180449.

In the same way I would like to thank the Instituto Nacional de Antropología e Historia (INAH) for the loan of the semi-fossil sample (C.A.401-36/0360). I also acknowledge the help granted by Juan José Lozano in the revision of this work.

Preface

Different digital non-contact optical techniques have recently been developed, becoming popular for shape recovery and fracture or deformation of three-dimensional (3D) objects. These techniques have been used for three-dimensional imaging of biological objects, but most of them interact and damage the surface of the object. Given the historical interest in digital preservation of morphology of fossil and taking into account that deoxyribonucleic acid (DNA) conservation is essential in studies of evolutionary genetics and the dating of evolutionary events, a non-contact technique is essential to avoid the risk of contaminating it with additional chemical agents or modern material and to preserve the topography of the same. The method of 3D profile measurement used is phase measurement profilometry by fringe projection. In the fringe-projection technique, a reference optical grating is first generated and then projected onto the surface of interest. The physical record represents the best way to document radiation and morphological transitions for taxonomic study groups. For this reason, we made the processing of semi-fossilized materials according to protocols for both, the management of old samples (genetically tested) and for optical measurements. For a given optical set-up, the distribution of the reference grating is perturbed in accordance with the profile of the test surface, thereby enabling direct derivation of surface profiles from measurements of the perturbed fringe distribution. However, to achieve a reasonable accuracy when these images contain a large number of systematic or random errors, the application of different phase shifting algorithms (PSA) and even numerical approximations methods to acquire the topography from experimental images becomes a tedious task. Consequently, instead of using the numerical and time consuming traditional method, wherein each filtering processing deteriorates the quality of the

original data, it is essential to design a set of analytical filters. To tackle this problem, it is necessary to use a new method for generating phase filters that are optimized for each application; in this case, it refers to the use of structured white light to measure the topography in semi-fossilized materials. Particularly, the two-frame filter algorithm has many advantages to design phase filters for temporal phase shifting (TPS) in order to extract the wave. TPS can be used with different types of electromagnetic sources (e.g., X-rays, IR-laser); however, when applied in conjunction with a low power electromagnetic source, like visible light (in this case, white light), it has an advantage that has been greatly underestimated: given that it is a contrast method instead of a radiative one, it is significantly harmless when used to obtain images of the surface of biological samples, as opposed to other sources such as X-ray and IR-light that irreversibly damage DNA and induce mutations. The two-frame formalism applied in TPS solves the problem that involves the calculation and design of a filter for any number of steps, tunable to any desired frequency, and it minimizes certain types of errors that influence the behavior of phase shifting filters to recover the phase. The principal advantage of the two-frame formalism is that it is able to find the accurate and analytic Fourier response equation, by tuning the filter according to the requirements of any real TPS experiment setup. The two-frame formalism also provides the analytical data expression, and allows us to analyze them based on the fact that there is no ideal filter with a finite number of steps due to the different variations of the TPS experiments. Hence, errors such as bias and detuning are compensated, fading them until their influence on the phase is almost zero, rather than eliminated in most of the cases.

In this thesis, several eight-frame algorithms for their use in phase shifting profilometry and their application for the analysis of semi-fossilized materials are presented. All algorithms are obtained from a set of two-frame algorithms and designed to compensate common errors such as phase shift detuning and bias errors. The processed images make it possible to obtain the distribution of height (topography) of the object, with the advantage that this type of structured

light is ideal for retaining the intrinsic biological properties of fossils (this property could be especially useful in cases where it is crucial to obtain high quality images from biological samples that include sensitive molecules, as is the case with ancient DNA). In addition, because the availability of fossil samples is limited (fossilization is a rare phenomenon, thought to preserve only 1 to 5% of total biodiversity) and fossils preserve key biological information, it is essential to conserve as many morphological features as possible (e.g., teeth and mandibles for rodents). This work provides the tools to create a 3D database for the study of morphology of semi-fossilized specimens using an optical nondestructive testing technique. The implementation of protocols and computational algorithms developed in this study in conjunction with various optical methods can be used in studies of systematics, evolution, ecology, genetics and geographical distribution for various biological groups.

Keywords: metrology, interferometry, fringe analysis, phase shifting interferometry, phase shift algorithm, fossils, phase shifting profilometry, two-frame, fringe projection profilometry, phase shifting, error filters, image reconstruction.

List of Acronyms and Abbreviations

aDNA	Ancient deoxyribonucleic acid
CCD	Charge-coupled device
DBE	Detuning and bias errors
DNA	Deoxyribonucleic acid
DVP	Digital video projector
FTM	Fourier transform method
FPP	Fringe projection profilometry
MDE	Mainly detuning error
MBE	Mainly bias error
PCR	Polymerase chain reaction
PG	Photogrammetry
PSA	Phase shifting algorithm
PSI	Phase shifting interferometry
PSP	Phase shifting profilometry
SNR	Signal-to-noise ratio
SEM	Scanning electron microscope
TPS	Temporal phase shifting
UV	Ultraviolet

Contents

List of figures

List of tables

Chapter 1

General Introduction

1.1 Introduction

The analysis of interferograms can be categorized in two methods: temporal methods (phase shifting) and spatial methods [1]. It is well known that in the temporal phase shifting (TPS) techniques, the existing algorithms exhibit considerable measurement inaccuracy unless phase shifts are precisely known. Accordingly, many efforts have been made in recent decades to establish effective error-compensating phase-extraction algorithms [2,3]. Most of the existing phase-shifting algorithms are based on the assumption that the phase-shift applied to each pixel of the intensity frame is a known constant value. However, it may be very difficult to achieve this in practice, mainly because one of the enduring problems with temporal phase-shifting algorithms (PSA) is precisely the phase-shift errors or miscalibration. By using more than three frames, it is possible to design algorithms to compensate the deterministic shift errors (such as nonlinearities of first, second and third order for the piezoelectric), and others like non-sinusoidal fringe profiles [1]. These TPS techniques are applied in the design of non-contact optical 3D-profiling instruments, which can be often used for the study of surface modifications of mammalian fossil bones. The main advantage of optical laser scanning of fossil and semi-fossil bones is that the laser's non-contact nature permits the analysis of a small fragile and poorly preserved surface [4]. Therefore, the stylus 3D-microprofiling technique has revealed several qualities that make it particularly suitable for the study of fossil and semi-fossil bones under atmospheric conditions, as they cause no alteration to the surface, to the objects.

In addition, complex surface features such as broadside inclinations, symmetry and micro-striations are accessible for quantitative evaluation, and features hidden by shallow overall relief are visually extracted [5]. Considering the importance in different research fields (as paleontology and biology) of having a full digital documentation of fossilized bones, for

example to compare morphological measurements, it is critical to have a method to obtain accurate digital three-dimensional images. Moreover, digital three-dimensional imaging becomes crucial for studies that involve the use of ancient deoxyribonucleic acid (aDNA) in which samples (semi-fossilized in this case) need to be completely pulverized to extract aDNA. Well preserved fossil samples, with minimum handling, are essential in order to obtain high quality aDNA. This provided the incentive to design phase filters that satisfy the requirements of the optical experimental setup.

The technique of fringe projection profilometry (FPP) is used for recovering surface topography. Nevertheless, the accuracy of this technique is limited by the presence of different systematic and random error sources, such as higher harmonics in the intensity signal, phase-shifter miscalibration, nonlinear response of the photodetectors, nonsinusoidal periodic waveforms, random intensity noise, speckle decorrelation, and vibration. All algorithms compensate for some kind of error, thus in the experiment we present, we calculated several filters with specific behaviors. As the errors cannot be completely eliminated but only minimized [1], the common technique to minimize systematic errors is the use of a quadrature filter insensitive to such errors [6-8]. There are already several methods to design quadrature filters and a large number of algorithms in the literature [6-13]. However, most of them only give a particular algorithm designed for a very specific phase step, which are not tuned on the ideal phase step. Hence, in this study we introduce several eight-frame filters with phase steps of $\pi/4$ that have not been reported. These algorithms are designed to compensate some systematic errors such as miscalibration and bias variation, which implies more accuracy and better signal recovery for eight step systems.

Today there are many non-destructive optical systems implemented in many areas of science and technology [14, 18]. Until now however, no efforts have been made to implement optical processing algorithms for a particular purpose and under very strict conditions, such as

the molecular study of semi-fossilized samples. Under this premise, this investigation explores some of the newest techniques to develop phase shifting algorithms for non-contact techniques and satisfies this need in the field of metrology.

The present work offers a new set of eight-frame algorithms for phase extraction, which are obtained from a set of two-frame filters and are designed to achieve the best signal-to-noise ratio (SNR), capable of minimizing, and even compensate for most of the systematic errors as quadrature and detuning errors. The algorithms are tested and their efficiency corroborated by using computer simulated fringe patterns and a simple fringe projection profilometry system for the analysis of semi-fossilized samples.

1.2 Overview

This section describes the distribution of topics addressed in each of the chapters of the thesis, and provides a brief description of the content of each chapter.

Chapter 2 provides the background related to the study of FPP; a mention is made of the variations among phase shifting interferometry, temporal phase shifting and fringe projection profilometry. It presents the optical profilometry theory and the types of schemes commonly used, and applications are mentioned that could be obtained with this scheme. In addition it should be mentioned that this part of the thesis also provides the relevant information on the development of different systems to compensate for several kinds of errors. Finally, this chapter describes some of the existing methods and techniques for phase shifting algorithms.

In chapter 3, by use of the two-frame formalism, a new set of analytical filters is calculated and a study performs the numerical analysis and evaluates the basic error

compensation of the filters. Furthermore, by mathematical analysis of the proposed algorithms, an evaluation and performance simulation for each filter response is performed and an optimal filter for FPP is determined. At the end of the chapter, a more specific algorithm for semi-fossilized materials is proposed for TPS systems.

The chapter 4 focuses on the application of the new algorithms proposed for processing images in fringe projection profilometry systems. It shows the advantages obtained by this novel scheme and presents an analysis of the results obtained for semi-fossilized samples. This part presents both experimental and numerical results and a FPP system in the laboratory to acquire images and corroborate the results produced by the simulations. Then, to conclude the chapter, and after developing simulations of the detuning and bias error corrections in 2D and 3D, experimental and numerical results are presented and discussed.

Finally, chapter 5 presents the final conclusions of this part of the work. The results obtained in this work are sorted and the possible applications that can be developed using the proposed study scheme and its future perspectives are mentioned.

References

1. J. F. Mosiño, D. Malacara Doblado, and D. Malacara Hernández, "A method to design tunable quadrature filters in phase shifting interferometry," Opt. Express **17**, 15772-15777 (2009).

2. K. Larkin, "A self-calibrating phase-shifting algorithm based on the natural demodulation of two-dimensional fringe patterns," Opt. Express **9**, 236-253 (2001).

3. P. D. Ruiz, J. M. Huntley, and G. H. Kaufmann, "Adaptive phase-shifting algorithm for temporal phase evaluation," J. Opt. Soc. Am. A **20**, 325-332 (2003).

4. H. Katterwe, "Modern approaches for the examination of toolmarks and other surface marks," Forensic Sci. Rev. **8**, 45–72 (1996).

5. T. M. Kaiser, and H. Katterwe, "The application of 3D-microprofilometry as a tool in the surface diagnosis of fossil and sub-fossil vertebrate hard tissue. An example from the pliocene upper laetolil beds, Tanzania," Int. J. Osteoarchaeol. **11**, 350–356 (2001).

6. Y. Surrel, "Design of algorithms for phase measurements by the use of phase stepping," Appl. Opt. **35**(1), 51–60 (1996).

7. D. W. Phillion, "General methods for generating phase-shifting interferometry algorithms," Appl. Opt. **36**, 8098-8115 (1997).

8. J. Schmit, and K. Creath, "Extended averaging technique for derivation of error-compensating algorithms in phase-shifting interferometry," Appl. Opt. **34**(19), 3610–3619 (1995).

9. K. Creath, "Temporal phase measurement methods," in *Interferogram Analysis*, D. W. Robinson and G. T. Reid, eds. (Institute of Physics, Bristol, 1993).

10. J. M. Huntley, "Automated Analysis of Speckle Interferograms," in *Digital Speckle Pattern Interferometry and Related Techniques*, P. K. Rastogi,ed. (Wiley, New York, 2001).

11. Y. Surrel, "Phase stepping: a new self-calibrating algorithm," Appl. Opt. **32**, 3598-3600 (1993).

12. K. Creath, and J. Schmit, "N-point spatial phase measurement techniques for nondestructive testing," Opt. Lasers Eng. **24**, 365–379 (1996).

13. K. Hibino, B. F. Oreb, D. I. Farrant, and K. G. Larkin, "Phase-shifting algorithms for nonlinear and spatially nonuniform phase shifts," J. Opt. Soc. Am. A **14**, 918-930 (1997).

14. Y. Hu, J. Xi, J. Chicharo, and Z. Yang, "Improved three-step phase shifting profilometry using digital fringe pattern projection," International Conference on Computer Graphics, Imaging and Visualization, 161-167 (2006).

15. S. Gorthi and P. Rastogi, "Fringe projection techniques: whither we are?," Opt. Lasers Eng **48**, 133-140 (2010).

16. G. Guidi, M. Pieraccini, S. Ciofi, V. Damato, J. Beraldin, and C. Atzeni, "Tridimensional digitizing of Donatello's Maddalena," IEEE Int. Conf.Image Processing **1**, 578–581 (2001).

17. G. S. Spagnolo, D. Ambrosini, and D. Paoletti, "Low-cost optoelectronic system for three-dimensional artwork texture measurement," IEEE Trans.Image Processing **13**(3), 390-396 (2004).

18. G. Sansoni, and F. Docchio, "3-D optical measurements in the field of cultural heritage: The case of the Vittoria Alata of Brescia," IEEE Trans. Instrumentation and Measurement **54**(1), 359-368 (2005).

Chapter 2

Non-contact optical techniques for shape measurement

2.1 Fringe projection profilometry, a non-contact optical technique

Technology for 3D information recovery has been subject to research considerably in recent years proposing many different systems for this purpose. A common classification for these systems is based on how the information of an object is acquired, dividing them into contact and non-contact devices. Contact devices typically are expensive, slow and require calibration each time a measurement is performed. The non-invasive measurement techniques maintain mechanical characteristics of the measured object, which has many advantages of analysis, since it can make an unlimited number of measurements on the same object. Regarding non-contact techniques, the fringe projection technique stands out from other optical techniques due to its ease of implementation, non-invasive nature and the accuracy that can be obtained. This technique is based in the fact that by analyzing the pattern reflected from a surface under study, we can obtain the heights map of the surface to subsequently perform mathematical analysis over this map and get the topography. The fringe projection technique handles different kinds of methods to analyze the data and get the phase map. Based on the particular fringe analysis method used in the measurement, fringe projection techniques are classified as phase shifting profilometry (PSP), Fourier transform profilometry (FTP), wavelet transform profilometry (WTP), spatial filtering profilometry (SFP) etc. [13]. The correct fringe analysis is essential, since it significantly influences the overall performance of the fringe projection profilometry system in terms of number of images required, resolution and accuracy of measurement, computational requirements etc.

2.2 Phase measurement

Several fringe analysis methods have been developed to process the images from a fringe projection system and thus obtain the phase map. In general, they can be categorized in spatial and temporal ones. Their effective and successful application requires the presence of a sufficiently high frequency spatial carrier in spatial methods, and the acquisition of a number of images by projecting phase-shifted fringe patterns for the temporal methods. Some of the fringe analysis methods introduced in the context of fringe projection profilometry are Fourier transform method and numerous extensions of it [14-21], interpolated Fourier transform [22],regressive Fourier transform [23], windowed Fourier transform [24], multi-scale windowed Fourier transform [25, 26], one-dimensional and two-dimensional Wavelet transforms [27, 28], analysis using inverse cosine function [29], phase locked loop [30-32], spatial phase detection [33, 34], and phase-shifting methods [35-37]. For the purposes of this thesis, the Fourier transform and the phase shifting methods are explained below.

2.3 Fourier Transform method

The Fourier transform method (FTM) is widely used to obtain phase because the the information can be achieved from a single image. This method was reported by Takeda [14] and is based on transforming a fringe pattern to the Fourier domain (frequency domain) for the analyses [38-40]. Considering that a fringe pattern can be written as

$$g(x,y) = a(x,y) + b(x,y)\cos\left[2\pi f_0 x + \varphi(x,y)\right] \tag{2.1}$$

where $a(x,y)$ is the background illumination, $b(x,y)$ is the modulation and $\varphi(x,y)$ represents the desired phase. For the Fourier transform, we rewrite Eq. (2.1) as follows:

$$g(x,y) = a(x,y) + c(x,y)e^{i2\pi f_0 x} + c^*(x,y)e^{-i2\pi f_0 x} \tag{2.2}$$

where

$$c(x,y) = \frac{1}{2}b(x,y)e^{i\varphi(x,y)} \tag{2.3}$$

and c^* denotes the complex conjugated of c. Then, the Fourier transform of Eq. (2.2) with respect to x gives the Fourier spectra $G(f,y)$ as

$$G(f,y) = A(f_x,y) + C(f_x - f_0,y) + C^*(f_x + f_0,y) \tag{2.4}$$

The representation of this Fourier spectrum is shown in Fig. (2.1(a)):

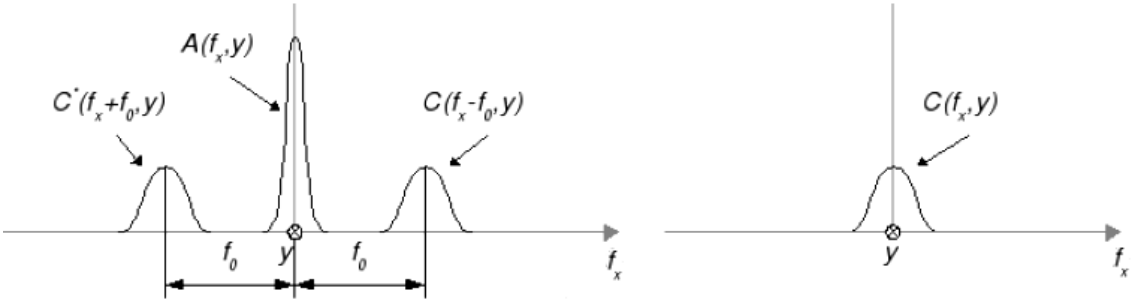

a) b)

Fig. 2.1: a) Spectra of the fringe pattern. b) Selected spectra transferred to the origin.

Using a filter any of the two spectra can be isolated and translated by f_0 towards the origin to remove the carrier and obtain $C(f_x,y)$ (Fig. 2.1(b)). Then the inverse Fourier transform of $C(f_x,y)$ with respect to x is computed and as a result the complex function $c(x,y)$ is obtained.

$$\log\left[c(x,y)\right] = \log\left[\frac{1}{2}b(x,y)\right] + i\varphi(x,y) \tag{2.5}$$

The phase $\varphi(x,y)$ is obtained by extracting the imaginary part which is separated of $b(x,y)$ in the real part. Finally, the phase is obtained by:

$$\varphi(x,y) = \tan^{-1}\left\{\frac{\mathrm{Im}\left[c(x,y)\right]}{\mathrm{Re}\left[c(x,y)\right]}\right\} \tag{2.6}$$

where Re and Im represents the real and imaginary part of $c(x,y)$.

2.4 Phase shifting profilometry

The phase shifting profilometry is one of the most commonly used non-contact methods for retrieving the three-dimensional (3D) shape information of objects. It offers the advantages of non-contact operation, full-field acquisition, high resolution, and fast data processing. For these reasons, the PSP, specifically as a fringe projection profilometry system (FPP), has become one of the most important 3D shape measurement methods [41]. In a FPP system, a series of straight vertically or horizontally oriented and equally spaced fringes are generated by computer and projected onto the surface of an object using a digital video projector (DVP). On the meanwhile, a CCD camera captures the intensity from the surface of the object for further processing. A typical FPP system is shown in Fig. 2.2.

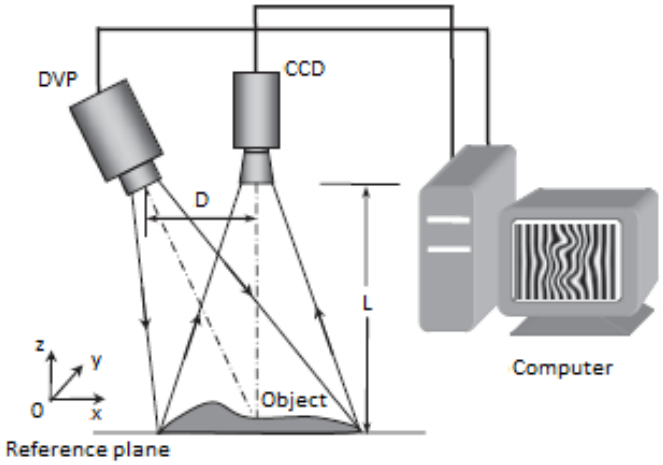

Fig. 2.2: A schematic diagram of a typical FPP system (L is the distance from the object to the camera and D is the distance between the CCD and the DVP).

By using the phase shifting method (PS), n-ths fringe patterns $I_n(x,y)$ (intensity patterns) are captured by the camera and which are commonly described as:

$$I_n(x,y) = a(x,y) + b(x,y)\cos\left[(2\pi/p)x + \varphi(x,y) + \theta n\right] \tag{2.7}$$

where n is the number of the phase-shifting steps $n = 1, \ldots, N$ (total number of images acquired); (x, y) denotes the coordinates of an arbitrary point in object; p is the period of the equally spaced fringes on the reference plane; $\varphi(x, y)$ is the phase map related to the object profile also called wrapped phase and, θ is the assigned phase shift value which is usually equal to $2\pi/N$ [42]. The numerical process to recover the wrapped phase from the set of captured images is called phase shifting algorithms (PSA). The correct design of this algorithm according to the specific setup determines the complexity and resolution of our results that, in few words, uses the intensity values obtained by shifting the fringes on the object to calculate the phase [43]. Subsequently, to make this phase map continuous, an unwrapping procedure is needed to remove the artificial discontinuities added by the FPP technique. The unwrapping techniques start from the fact that it is possible to estimate the neighboring pixel differences of the unwrapped phase when these

differences are less than π by adding an integral factor of *2π*. Then, using some mathematical methods is possible to obtain the data cloud points proportional to the physical sample analyzed [44]. Then, temporal carrier is calculated and subtracted from the phase map. Finally, the topography or profile is calculated by:

$$h(x, y) = I_0 \ \varphi(x, y) / \left[2\pi f_0 d + \varphi(x, y) \right] \tag{2.8}$$

where f_0 is the distance between the CCD camera and the reference plane, and d is the distance between the camera and the projector (Fig. 2.2).

Due to the intensity response of a FPP system, including the influence of the DVP [45], the object surface reflectivity, environment brightness, the CCD camera, etc., the fringe pattern will deviate from its ideal form. This method is not sensitive to the background and reflection factor of surfaces; nevertheless, one of the main problems with the existing algorithms for PSP is that retrieving the information of the fringes is considerable imprecisely unless the phase steps are well known.

Almost all the existing phase-shifting algorithms are based on the assumption that the phase-shift at all pixels of the intensity frame is equal and known. However, it may be very difficult to achieve this case in practice. Some phase shift miscalibrations could be avoided due digitally generated fringes. The accuracy of the phase measurement of a fringe pattern depends on systematic and random error sources located in the setup elements (hardware), since the variation of fringe visibility along the optical path is mathematically equivalent to the variation of phase-shift errors [46] as well as in the algorithms to calculate the phase (software). Several algorithms have been developed to calculate the phase of a fringe pattern. Some of this phase shifts algorithms (PSA) use intensity values that one obtains by shifting the phase of the intensity pattern to calculate the phase [43]. The nonlinear characteristic of a FPP system inevitably introduces and additional phase error that can be compensated by using a large number of phase shifts fringe patterns [47]. However, phase shifting usually requires a minimum

of two phase-shifted images for extraction of phase information, and the phase retrieval from multi-frame fringe patterns is time and space consuming and will reduce the speed of shape measurement [48].

2.5 Description of some phase shifting algorithms

Many authors have developed a variety of methods for PSA [49, 50], such as averaging with existing algorithms and solving for the roots of a characteristic polynomial [51], data-sampling windows, Fourier analysis, least-squares, etc. The use of the TPS is based on the addition of a careful phase change that is projected to the target surface. It also involves analyzing data from each pixel independently of all other pixels in the frame. This technique is based on the work of Carré as shown in Eq. (2.9). Carré algorithm is a variation of the four-step algorithm, but instead of requiring that the data be collected at $\pi/4$ increments, the reference phase shift between measurements is treated as an unknown and solved for in the analysis [50]; in other words, it considers that the problem of phase-shifter miscalibration is dealing with treating the phase shift as one more unknown variable.

$$\tan(\varphi)=\left[\frac{\sqrt{\left[I(0)-I(3)+I(1)-I(2)\right]\left\{3\left[I(1)-I(2)-I(0)+I(3)\right]\right\}}}{I(1)+I(2)-I(0)-I(3)}\right] \tag{2.9}$$

Although this algorithm to recover the phase is useful for phase shifts that vary over a considerable range, it is susceptible to high-order harmonics in the signal [52]. More than three frames measurements give extra degrees of freedom to design phase algorithms that are insensitive to these real-world effects [51]. Like binary structured patterns, more fringe images can be used to achieve higher accuracy, but this slows down the measurement speed [53]. This

could be a problem when we want to reach real-time 3D imaging and a small number of fringe images (fringe patterns) are typically used, but in this work, we pretend to achieve maximum precision and accuracy by compensating the most common errors. Another technique consists in the (N+1)-bucket method, which is based on the fact that we need a specific value of the shift [54], as in the conventional N-bucket algorithm [55] given by

$$\tan(\varphi)=\left[\frac{\sum_{n=0}^{N-1} I(n)\sin\left(\frac{2\pi n}{N}\right)}{\sum_{n=0}^{N-1} I(n)\cos\left(\frac{2\pi n}{N}\right)}\right] \tag{2.10}$$

where $I(n)$ is the recorded intensity for a phase shift of $n\alpha$ ($\alpha=2\pi/N$); N is the number of fringe patterns recorded and φ is the desired phase map. These algorithms are widely used because they have some advantages as that a large quantity of images could be acquired to improve the signal-to-noise ratio and they are insensitive to some phase shift miscalibrations. However, these two algorithms are affected widely by the presence of systematic errors, like harmonics in the signal, high frequencies environmental perturbations in the fringes, errors based on the bias (produced i.e. by the piezoelectric transducer used to achieve the phase shifting), a detuning, and optical experimental errors such as the camera and its resolution used in the experiment. It is known that linear phase shift miscalibrations and nonlinear sensitivity of the piezoelectric device introduce errors in phase measurement. This study reveals that, out of the various algorithms proposed for compensating such errors, most algorithms are suitable for only one of these two error sources. An eight-frame algorithm widely used is [56],

$$\tan(\varphi)=\left(\frac{I_2-I_4+I_6-I_8}{I_1-I_3+I_5-I_7}\right) \tag{2.11}$$

Finally, the (N+3)-bucket algorithm reported by Hibino et al. is expressed by [46]

$$\tan(\varphi) = \left[\frac{2I_1 - I_2 - 6I_3 - 3I_4 + 3I_5 + 6I_6 + I_7 - 2I_8}{3\sqrt{3}(I_2 - I_4 - I_5 + I_7)} \right] \tag{2.12}$$

Each of these filters has unique characteristics that compensate for certain types of errors in the optical techniques. Referring to such errors, there is a wide range of sources of error that affect the accuracy of phase measurements which can be divided into three categories: a) Systematic error, including errors in the phase shifting process, nonlinearities in the photodetectors, amplitude and frequency stability of the source, etc.; b) Random errors, including vibrations of the optical system, turbulence in the air, etc.; c) Aberrations and defects in the optical arrangement. Then, an effective algorithm developed for that purpose is needed. In this work, a set of four practical eight-frame algorithms for fringe projection profilometry were designed to prevent and even compensate several systematic errors including random noise for applications that include rough and semi fossilized materials. A more detailed explanation of some of the principal errors involved in optical measurements is shown below.

2.6 Phase unwrapping

The recovered/estimated phase from the deformed fringe pattern by using most of the aforementioned fringe analysis methods is mathematically limited to the interval $(-\pi, \pi)$ corresponding to the principal value of arctan function. In general the true phase may range over an interval greater 2π in which case the recovered phase contains artificial discontinuities. The process of determining the unknown integral multiple of 2π to be added to each pixel of the wrapped phase map to make it continuous by removing the artificial 2π discontinuities added is referred to as phase unwrapping. Normal phase unwrapping is carried out by comparing the

neighboring pixels and adding or subtracting 2π to bring the relative phase between the two pixels into the range of $-\pi$ to $+\pi$. This process can be seen in Fig. 2.3.

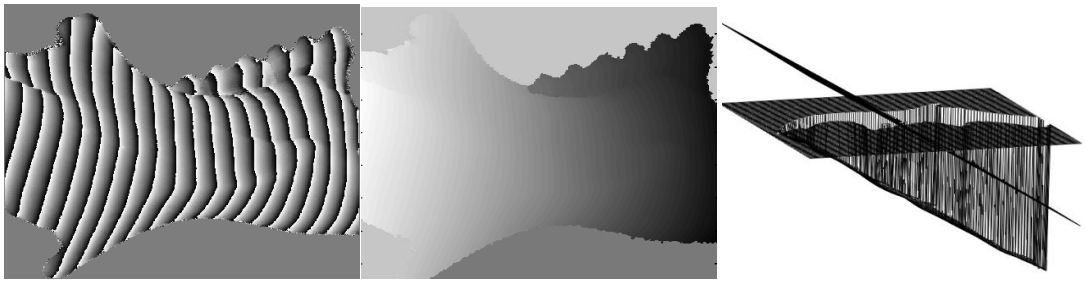

(a) (b) (c)

Fig. 2.3: Examples of: (a) wrapped phase, (b) unwrapped phase, and (c) phase carrier compensation.

The unwrapped phase is obtained by using techniques involving an unwrapping algorithm, as the flood-guide technique [44]. The unwrapping of the phase is a complex process and techniques start from the fact that it is possible to estimate the neighboring pixel differences of the unwrapped phase when these differences are less than π [57] by adding an integral multiple of 2π. Using some mathematical methods [44] is possible to obtain the cloud data points proportional to the physical sample analyzed. Then, temporal carrier is calculated and subtracted [58] to finally obtain the reconstructed topography of the fossil in the form of a cloud of points.

2.7 Systematic errors in phase shifting

Phase shifting profilometry (PSP) technique is widely used as a 3D shape measurement technique due to its robustness and accuracy. However, PSP requires multiple fringe pattern

images to be projected onto an object and a reference plane to calculate the phase value, and also the object must maintain motionless when the measurement is taken. If the object moves during the measurement, significant errors will be introduced when calculating the phase value. A systematic error associated with the fact that a measured value contains an offset is called bias error. This kind of error is very common in optics measurements.

2.7.1 High order harmonics

In practice, signals acquired from an optical system not always are pure signals, as a sine wave recovered from an interferogram. Higher harmonics can be produced for many reasons as non-linearities in the photodetector or the saturation in the pixels in certain environments [59]. Consider the case of sampling the function $I(t)$, if the frequency is greater that the Nyquist frequency $k_t = N/2$, the harmonics will be aliased on the range $(-N/2, N/2)$. For a harmonic component with frequency of q times the fundamental, according to the Nyquist theorem, the spectra peaks at $k_t = jN \pm q$.

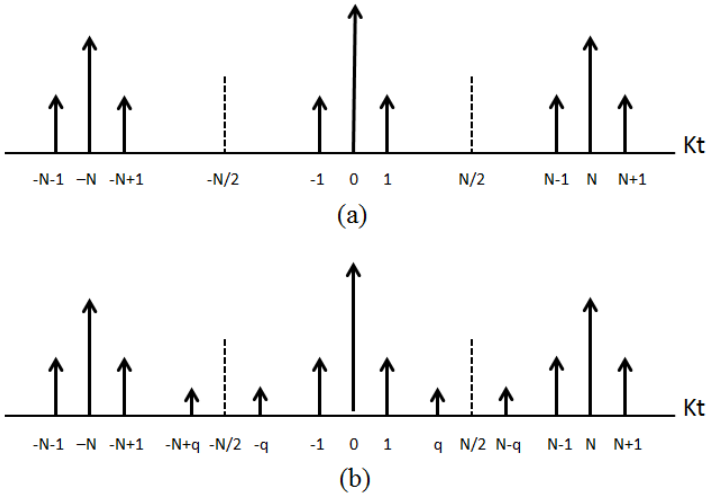

Fig. 2.4: (a) Fourier transform of a signal. (b) Harmonics at a frequency q times the fundamental.

2.7.2 Phase shifter miscalibrations

A single movement of the sample in an optical system while a series of interferograms are being acquired results in phase shifts that derivate from the nominal value, and this is equivalent to a miscalibration of the phase shifter. This implies that the interferograms recorded have a carrier frequency different to the original one by an error ε [59,60]. When the signal frequency and the reference frequency are not equal, the system contains a phase shifting detuning error.

2.7.3 Vibration

Vibrations and other environmental disturbances (such as air currents) can cause significant phase measurements errors, such as the detuning error. The use of high speed cameras or pulsed lasers which are capable to take an image in a short lap of time will often allow data to be obtained from non-optimal or time-dependent conditions. [59].

2.7.4 Random errors

Intensity noise due to variation in the light source or electronic noise in the camera of an optical system will result in random errors in the measures phase. Surrel analyzed some phase-shifting algorithms and showed in the presence of random intensity errors, $\tilde{\varphi}$ has an average standard derivation σ_{φ} given by

$$\sigma_{\varphi}^2 = \frac{2\sigma_1^2}{\eta^2 M I_M^2} \tag{2.13}$$

where σ_1 is the standard derivation intensity and η is a numerical factor. For most algorithms until now, η ranged from 0.8 to 1, indicating that there is a little influence of the selected algorithm on σ_{φ}.

References

1. F. Chen, G. Brown, and M. Song, "Overview of 3-D shape measurement using optical methods," Opt. Eng. **39**, 10-22 (2000).

2. W. Schreiber, and G. Notni, "Theory and arrangements of self-calibrating whole-body 3-D measurement systems using fringe projection technique," Opt. Eng. **39**, 159-169 (2000).

3. L. Salas, E. Luna, J. Salinas, V. Garcia, and M. Servin, "Profilometry by fringe projection," Opt. Eng. **42**, 3307-3314 (2003).

4. Q. Hu, P. Huang, Q. Fu, and F. Chiang, "Calibration of a three-dimensional shape measurement system," Opt. Eng. **42**, 487–93 (2003).

5. R. Legarda-Sáenz, T. Bothe, and W. Juptner, "Accurate procedure for the calibration of a structured light system," Opt. Eng. **43**, 464–471 (2004).

6. C. Tay, C. Quan, T. Wu,and Y. Huang, "Integrated method for 3-D rigid-body displacement measurement using fringe projection," Opt. Eng. **43**, 1152–1159 (2004).

7. J. Pan, P. Huang, and F. Chiang, "Color-coded binary fringe projection technique for 3-D shape measurement," Opt. Eng. **44**, 023606 (2005).

8. H. Guo, H. He, Y. Yu, and M. Chen, "Least-squares calibration method for fringe projection profilometry," Opt. Eng. **44**, 033603 (2005).

9. T. Peng, and S. Gupta, "Model and algorithms for point cloud construction using digital projection patterns," J. Comput. Inf. Sci. Eng. **7**, 372-381 (2007).

10. S. Zhang, X. Li, and S. Yau, "Multilevel quality-guided phase unwrapping algorithm for real-time three-dimensional shape reconstruction," Appl. Opt. **46**, 50-57 (2007).

11. S. Zhang, and S. Yau, "Generic nonsinusoidal phase error correction for three-dimensional shape measurement using a digital video projector," Appl. Opt. **46**, 36-43 (2007).

12. Z. Wang, D. Nguyen, and J. Barnes, "Some practical considerations in fringe projection profilometry," Opt. Lasers Eng. **48**(2), 218–225 (2010).

13. S. Gorthi and P. Rastogi, "Fringe projection techniques: whither we are?" Opt. Lasers Eng. **48**, 133–140 (2010).

14. M. Takeda, K. Mutoh, "Fourier transform profilometry for the automatic measurement of 3-D object shapes," Appl. Opt. **22**(24), 3977–3982 (1983).

15. J.-F. Lin, X.-Y. Su, "Two-dimensional Fourier transform profilometry for the automatic measurement of three-dimensional object shapes," Opt. Eng. **34**(11), 3297–3302 (1995).

16. X. Su, W. Chen, "Fourier transform profilometry: A review," Opt. Laser Eng. **35**(5), 263–284 (2001).

17. F. Berryman, P. Pynsent, J. Cubillo, “The effect of windowing in Fourier transform profilometry applied to noisy images,” Opt. Laser Eng. **41**(6), 815–825 (2004).

18. M. A. Gdeisat, D. R. Burton, M. J. Lalor, “Eliminating the zero spectrum in Fourier transform profilometry using a two-dimensional continuous wavelet transform,” Opt. Commun. **266**(2), 482–489 (2006).

19. P. J. Tavares, M. A. Vaz, “Orthogonal projection technique for resolution enhancement of the Fourier transform fringe analysis method,” Opt. Commun. **266**(2), 465–468 (2006).

20. S. Li, X. Su, W. Chen, L. Xiang, “Eliminating the zero spectrum in Fourier transform profilometry using Empirical mode decomposition,” J. Opt. Soc. Am. A **26**(5), 1195–1201 (2009).

21. M. Dai, Y.Wang, “Fringe extrapolation technique based on Fourier transformfor interferogram analysis with the definition,” Opt. Lett. **34**(7), 956–958 (2009).

22. S. Vanlanduit, J. Vanherzeele, P. Guillaume, B. Cauberghe, P. Verboven, “Fourier fringe processing by use of an interpolated Fourier-transform technique,” Appl. Opt. **43**(27), 5206–5213 (2004).

23. J. Vanherzeele, S. Vanlanduit, P. Guillaume, “Processing optical measurements using a regressive Fourier series: A review,” Opt. Laser Eng. **47**(3-4), 461–472 (2009).

24. Q. Kemao, “Windowed Fourier transform for fringe pattern analysis,” Appl. Opt. **43**(13), 2695–2702 (2004).

25. S. Zheng,W. Chen, X. Su, “Adaptive windowed Fourier transform in 3-D shape measurement,” Opt. Eng. **45**(6), 063601 (2006).

26. J. Zhong, H. Zeng, “Multiscale windowed Fourier transform for phase extraction of fringe patterns,” Appl. Opt. **46**(14), 2670–2675 (2007).

27. A. Dursun, S. Ozder, F. N. Ecevit, “Continuous wavelet transform analysis of projected fringe patterns,” Meas. Sci. Techn. **15**(9), 1768–1772 (2004).

28. J. Zhong, J. Weng, “Spatial carrier-fringe pattern analysis by means of wavelet transform: Wavelet transform profilometry,” Appl. Opt. **43**(26), 4993–4998 (2004).

29. K. Okada, E. Yokoyama, H. Miike, “Interference fringe pattern analysis using inverse cosine function,” Electronics and Communications in Japan, Part II: Electronics **90**(1), 61–73 (2007).

30. J. Kozlowski, G. Serra, “New modified phase locked loop method for fringe pattern demodulation,” Opt. Eng. **36**(7), 2025–2030 (1997).

31. D. Ganotra, J. Joseph, K. Singh, “Second- and first-order phase-locked loops in fringe profilometry and application of neural networks for phase-to-depth conversion,” Opt. Commun. **217**(1-6), 85–96 (2003).

32. M. A. Gdeisat, D. R. Burton, M. J. Lalor, "Fringe-pattern demodulation using an iterative linear digital phase locked loop algorithm," Opt. Laser Eng. **43**(7), 31–39 (2005).

33. S. Toyooka, Y. Iwaasa, "Automatic profilometry of 3-D di use objects by spatial phase detection," Appl. Opt. **25**(10), 1630–1633 (1986).

34. M. R. Sajan, C. J. Tay, H. M. Shang, A. Asundi, "Improved spatial phase detection for profilometry using a TDI imager," Opt. Commun. **150**(1-6), 66–70 (1998).

35. V. Srinivasan, H. C. Liu, M. Halioua, "Automated phase-measuring profilometry of 3-D di use objects," Appl. Opt. **23**(18), 3105–3108 (1984).

36. M. Chang, D. Wan, "On-line automated phase-measuring profilometry," Opt. Laser Eng. **15**(2), 127–139 (1991).

37. X. F. Meng, X. Peng, L. Z. Cai, A. M. Li, J. P. Guo, Y. R. Wang, "Wavefront reconstruction and three-dimensional shape measurement by two-step dc-term-suppressed phase-shifted intensities," Opt. Lett. **34**(8), 1210–1212 (2009).

38. Takeda M., Ina H., Kobayashi S., "Fourier-Transform Method of Fringe-Pattern Analysis for Computer-Based Topography and Interferometry", J. Opt. Soc. Am. **72**, 156-160 (1982).

39. D. Malacara, M. Servin, Z. Malacara, "Fourier Theory Review", Interferogram Analysis For Optical Testing, Second Edition, Taylor & Francis, 2005. Cap. 2.

40. Bone D.J., Bachor H.A., Sandeman R.J., "Fringe-Pattern Analysis Using a 2-D Fourier Transform," Appl. Opt. **25**, 1653-1660 (1986).

41. Yanjun Fu and Qian Luo, "Fringe projection profilometry based on a novel phase shift method," Opt. Express **19**, 21739-21747 (2011).

42. Ma, S., Quan, C., Zhu, R., Tay, C.J. "Investigation of phase error correction for digital sinusoidal phase-shifting fringe projection profilometry," Opt. Laser Eng **50**, 1107-1118 (2012).

43. Rathjen, C. 1995 Statistical properties of phase-shift algorithms. *Journal of the Optical Society of America A* **12**, 1997-2008.

44. Ghiglia, D.C. & Pritt, M.D. 1998 *Two-dimensional phase unwrapping theory, algorithms, and software*, 1st edn. USA. John Wiley & Sons, Inc.

45. Y. Hu, J. Xi, J. Chicharo, and Z. Yang, "Improved three-step phase shifting profilometry using digital fringe pattern projection," in IEEE International Conference on Computer Graphics, Imaging and Visualisation, 161–167 (2006).

46. Kenichi Hibino, Bob F. Oreb, David I. Farrant, and Kieran G. Larkin, "Phase-shifting algorithms for nonlinear and spatially nonuniform phase shifts," J. Opt. Soc. Am. A **14**, 918-930 (1997).

47. B. Pan, Q. Kemao, L. Huang, and A. Asundi, “Phase error analysis and compensation for nonsinusoidal waveforms in phase-shifting digital fringe projection profilometry,” Opt. Lett. **34**, 416-418 (2009).

48. Fujun Yang and Xiaoyuan He, “Two-step phase-shifting fringe projection profilometry: intensity derivative approach,” Appl. Opt. **46**, 7172-7178 (2007).

49. J. A. N. Buytaert and J. J. J. Dirckx, “Study of the performance of 84 phase-shifting algorithms for interferometry,” J. Opt. **40**(3), 114–131 (2011).

50. D. Malacara, Optical shop testing, 3rd. Edition, (J. Wiley and Sons Inc., Hoboken, New Jersey, 2007).

51. D. W. Phillion, “General methods for generating phase-shifting interferometry algorithms,” Appl. Opt. **36**, 8098-8115 (1997).

52. K. Creath, “Temporal phase measurement methods,” in Interferogram Analysis, D. W. Robinson and G. T. Reid, eds. (Institute of Physics, Bristol, 1993).

53. N. Karpinsky and S. Zhang, “High-resolution, real-time 3D imaging with fringe analysis,” J Real-Time Image Proc. **7**, 55-66 (2012).

54. J. M. Huntley, “Automated Analysis of Speckle Interferograms,” in *Digital Speckle Pattern Interferometry and Related Techniques*, P. K. Rastogi, ed. (Wiley, 2001).

55. Y. Surrel, “Phase stepping: a new self-calibrating algorithm,” Appl. Opt. **32**(19), 3598–3600 (1993).

56. K. Creath and J. Schmit, “N-point spatial phase measurement techniques for nondestructive testing,” Opt. Lasers Eng. **24**(5-6), 365–379 (1996).

57. A. Kattoush, “A new recurrent approach for phase unwrapping,” Int J Appl Sci Eng. **3**(2), 135–143 (2005).

58. K. Gasvik, “Optical Metrology”, 3rd ed. (Wiley, 2002).

59. *“Digital Speckle Pattern Interferometry and Related Techniques,”* P. K. Rastogi, ed. (Wiley, England, 2001).

60. Y. Surrel, "Additive noise effect in digital phase detection," Appl. Opt. **36**, 271-276 (1997).

Chapter 3

Proposal of new phase shifting algorithms

3.1 Two-frame algorithm to design quadrature filters

In phase shifting interferometry the ideal intensity $I(x,y,t)$ for k=1, 2, 3… M of each interferogram recorded by a CCD detector can be expressed as [5-7, 10-13]:

$$I(x,y,t) = a(x,y) + b(x,y)\cos\left[\varphi(x,y) + \omega_0 t\right] \tag{3.1}$$

where, x and y denote the pixel position; $a(x,y)$ is the background illumination; $b(x,y)$ is the contrast of interference fringes (amplitude), and $\varphi(x,y)$ represents the phase. Meanwhile, the temporal carrier ω_0 is a linear phase shift among this set of interferograms and it is determined by how fast the phase reference wave is changing.

Assuming an algorithm with order M and tuned onto the left side of the frequency axis in Fig. 2.1, the estimated phase of a quadrature filter order M is given by [5-7, 14-19],

$$\tan(\varphi) = \frac{\sum_{k=1}^{M} b_k I_k}{\sum_{k=1}^{M} a_k I_k} = \frac{\left[b_1\ b_2\ \ldots\ b_M\right]\vec{I}}{\left[a_1\ a_2\ \ldots\ a_M\right]\vec{I}} = \frac{N\vec{\mathbf{I}}}{D\vec{\mathbf{I}}} \tag{3.2}$$

It should be noticed that $\vec{\mathbf{I}} = \left[I_1\ I_2\ \ldots\ I_M\right]^T$ is the column vector of frames, and N and D are the desired numerator and denominator row vectors. In this case, for a symmetrical filter the corresponding temporal impulse response $h(t)$ is given by [16-19]

$$h(t) = \sum_{k=1}^{M} a_k\left[\delta(t-p)\right] + i\sum_{k=1}^{M} b_k\left[\delta(t-p)\right] = D\vec{\delta} + iN\vec{\delta} \tag{3.3}$$

where $i = \sqrt{-1}$, $p = (2k - M - 1)\alpha/2$ and $\vec{\delta}$ is a column vector where each element is $\delta(t-p) = \vec{\delta}_p$. That is, from the scalar vectors N and D, the Eqs. (3.2) and (3.3) are recovered easily. In the previous work it was proved that the Fourier transform of $h(t)$ is the real function $H(\omega)$ [17, 18]. For an α step, any quadrature filter satisfies the two conditions: $H(0) = 0$;

$H(\alpha)=0$. That is, the filter cuts off both $\omega=0$ and $\omega=\alpha$ frequencies. Therefore, the condition for a filter tuned onto the right side and insensitive to the $m-th$ order phase shift detuning error is [5-7, 14-17]

$$H'(\alpha)=0,\quad H''(\alpha)=0,\quad H'''(\alpha)=0,\quad ...,\quad H^{m}(\alpha)=0 \tag{3.4}$$

Assuming that the Fourier transform of a filter can be factorized in two functions such as $H(\omega)=H_1(\omega)H_2(\omega)$, where $H_1(\omega)$ and $H_2(\omega)$ are the Fourier transforms of $h_1(t)=D_1\vec{\delta}+iN_1\vec{\delta}$ and $h_2(t)=D_2\vec{\delta}+iN_2\vec{\delta}$ which are an *n* and *m* order filters respectively, the individual estimated phases φ_1 and φ_2 are given by

$$\tan(\varphi_1)=\frac{N_1\vec{\mathbf{I}}}{D_1\vec{\mathbf{I}}},\ \text{and}\ \tan(\varphi_2)=\frac{N_2\vec{\mathbf{I}}}{D_2\vec{\mathbf{I}}} \tag{3.5}$$

Hence, the desired filter $h(t)$ is obtained from the expression $h(t)=h_1(t)*h_2(t)$, where "*"denotes the temporal discrete convolution, and $h(t)$ becomes,

$$h(t)=\left[D_1\vec{\delta}+iN_1\vec{\delta}\right]*\left[D_2\vec{\delta}+iN_2\vec{\delta}\right]=\left[D_1*D_2-N_1*N_2\right]\vec{\delta}+i\left[N_1*D_2+D_1*N_2\right]\vec{\delta} \tag{3.6}$$

and this expression corresponds with the estimated phase φ and given by

$$\tan(\varphi)=\frac{N\vec{I}}{D\vec{I}}=\frac{\left[N_1*D_2+D_1*N_2\right]\vec{\mathbf{I}}}{\left[D_1*D_2-N_1*N_2\right]\vec{\mathbf{I}}} \tag{3.7}$$

that is, the convolution can be represented as

$$\frac{N}{D}=\left(\frac{N_1}{D_1}\right)*\left(\frac{N_2}{D_2}\right)=\frac{\left[N_1*D_2+D_1*N_2\right]}{\left[D_1*D_2-N_1*N_2\right]} \tag{3.8}$$

In other words, as mentioned before, a new $(n+m-1)$ frame filter from two individual filters is obtained. Likewise, the design of a tunable quadrature filter is seen as an algebraic problem without the use of Fourier formalisms. The convolution properties allow this case to be extended for three or more filters. The design of a quadrature filter order *M* implies that only *M*-1

parameters are free, two of which are the quadrature conditions and the other *M*-3 [8] are used to compensate some of the errors described in chapter 2.

3.2 Family of symmetrical eight-frame filters

Offset errors of different experiment requires different filters, for example, in the case of eight steps, a problem that is needed to meet and after the experiment and analyze different filters was completed in an ideal filter for this case. However, the number of filters in the literature very is extensive and they are limited in the way, not tunable and not suited to all experiments. Then, a filter that is tunable and can be used under the experimental conditions to be evaluated is preferred. The error equations and how to calculate compensated filters already have been given [14-17]. Then, an analytic expression is obtained through the convolution of a set of two-frame algorithms. From [20] if Fourier response is real, two-frame filter formalism can be used. Consequently, to design a family of eight frame phase shift algorithm with symmetric coefficients considering the estimated phase of a quadrature filter of order M is given by [8, 20]

$$\tan(\varphi)=\frac{\sum_{k=1}^{M} b_k I_k}{\sum_{k=1}^{M} a_k I_k}=\frac{\begin{bmatrix} b_1 & b_2 & \dots & b_M \end{bmatrix}\vec{\mathbf{I}}}{\begin{bmatrix} a_1 & a_2 & \dots & a_M \end{bmatrix}\vec{\mathbf{I}}}=\frac{N\,\vec{\mathbf{I}}}{D\,\vec{\mathbf{I}}} \tag{3.9}$$

It should be noticed the vector notation where, $\vec{\mathbf{I}}=[I_1 \quad I_2 \quad \dots \quad I_M]^T$ is the column vector of frames, φ is the phase with the desired shape information, and *N*, *D* are the desired numerator and denominator row vectors with the coefficients of the filter to be calculated. When the

Fourier response of the filters becomes real for $\theta_T = 0$ give us the ratio *N/D* corresponding to the filter algorithm with is given by

$$\frac{N}{D} = \underset{k=1}{\overset{M-1}{\Omega}} R(\alpha_k, 0) = \underset{k=1}{\overset{M-1}{\Omega}} \left\{ \frac{\cos(\alpha_k / 2)[1, \quad -1]}{\sin(\alpha_k / 2)[1, \quad 1]} \right\} \tag{3.10}$$

where Ω denotes a convolution operator introduced in [8, 20]. Eight-frame filters have seven free parameters available to design a mathematical expression that fits systematic errors and adequately compensate them. Therefore, for the general case of an eight frame filter *M=8*, and the ratio *N/D* becomes,

$$\frac{N}{D} = \underset{k=1}{\overset{7}{\Omega}} \left\{ \frac{\cos(\alpha_k / 2)[1, \quad -1]}{\sin(\alpha_k / 2)[1, \quad 1]} \right\} \tag{3.11}$$

To expand the last expression, the first step is to choose a set of arbitrary steps $\alpha = \{ \alpha_1, \alpha_2, \alpha_3 ... \alpha_7 \}$ (cuts-offs). For the desired response, an eight-frame algorithm is given by the following set of the cut-off frequencies with seven free parameters to choose. An important consideration is to choose only two tunable cut-off frequencies a, b and the symmetry of the steps, so that $\alpha = \{ 0, \pi/2, \pi, a, \pi - a, b, \pi - b \}$

$$\frac{N}{D} = \frac{[1 \quad -1]}{[0 \quad 0]} * \frac{\cos(a/2)[1 \quad -1]}{\sin(a/2)[1 \quad 1]} * \frac{\cos(b/2)[1 \quad -1]}{\sin(b/2)[1 \quad 1]} * \frac{[1 \quad -1]}{[1 \quad 1]} * \frac{\cos(a/2)[1 \quad -1]}{\sin(a/2)[1 \quad 1]} * \frac{\cos(b/2)[1 \quad -1]}{\sin(b/2)[1 \quad 1]} * \frac{[0 \quad 0]}{[1 \quad 1]} \tag{3.12}$$

Finally, the expression of the desired phase becomes

$$\tan(\phi) = \frac{N \vec{\mathbf{I}}}{D \vec{\mathbf{I}}} = \frac{b_1 I_1 + b_2 I_2 + b_3 I_3 + ... + b_8 I_8}{a_1 I_1 + a_2 I_2 + a_3 I_3 + ... + a_8 I_8} \tag{3.13}$$

where the coefficients of the numerator and the denominator above become (with two arbitrary tunable cut-off frequencies)

$$a_1 = 1 \tag{3.14}$$

$$a_2 = -2\sin(a) - 2\sin(b) - 1 \tag{3.15}$$

$$a_3 = -2\sin(a) - 4\sin(a)\sin(b) - 2\sin(b) - 3 \tag{3.16}$$

$$-a_4 = -4\sin(a) - 4\sin(a)\sin(b) - 4\sin(b) - 3 \tag{3.17}$$

where $a_1 = a_8 = -b_1 = b_8$, $a_2 = a_7 = b_2 = -b_7$, $a_3 = a_6 = -b_3 = b_6$ and $-a_4 = -a_5 = -b_4 = b_5$. Then, from [8] the corresponding Fourier response is

$$H(\omega) = (-2)^7 \prod_{i=1}^{N-1} \sin\left(\frac{\omega_i - \omega_0}{2}\right) \tag{3.18}$$

$$H(\omega) = (-2)^7 \sin\left(\frac{\omega}{2}\right)\sin\left(\frac{\omega-\pi}{2}\right)\sin\left(\frac{\omega-\pi/2}{2}\right)\sin\left(\frac{\omega-a}{2}\right)\sin\left(\frac{\omega-b}{2}\right)\cos\left(\frac{\omega+a}{2}\right)\cos\left(\frac{\omega+b}{2}\right) \tag{3.19}$$

However, in practice, we tuned in only one cut-off frequency. Then, from Eq. (3.13), we have the particular case $b = a$, and the filter becomes more robustness to the detuning error,

$$a_1 = 1 \tag{3.20}$$

$$a_2 = -4\sin(a) - 1 \tag{3.21}$$

$$a_3 = 2\cos(2a) - 4\sin(a) - 5 \tag{3.22}$$

$$-a_4 = 2\cos(2a) - 8\sin(a) - 5 \tag{3.23}$$

where $a_1 = a_8 = -b_1 = b_8$, $a_2 = a_7 = b_2 = -b_7$, $a_3 = a_6 = -b_3 = b_6$ and $-a_4 = -a_5 = -b_4 = b_5$; then the Fourier behavior becomes

$$H(\omega) = 32\sqrt{2}\sin(\omega)\left[\sin\left(\frac{\omega}{2}\right) - \cos\left(\frac{\omega}{2}\right)\right]\sin^2\left(\frac{\omega-a}{2}\right)\cos^2\left(\frac{\omega+a}{2}\right) \tag{3.24}$$

It should be noticed that each filter corresponds to a symmetrical eight-frame algorithm, and each one of these filters contains specific characteristics that compensate for several kinds of errors presented when recovering the wrapped phase. Therefore, a family of new filters for some representative error cases is generated. These cases are shown in Table 1. It should be noticed that each filter corresponds to a symmetrical eight-frame algorithm, and its specific characteristics involve the compensation of several kinds of errors that can be corrected by recovering the wrapped phase.

Table 3.1: Family of tunable eight-frame filters for TPS.

	a	b	N / D	Plot of the zeros of the characteristic polynomials
1	0	0	$\frac{[-1 \quad -1 \quad 3 \quad 3 \quad -3 \quad -3 \quad 1 \quad 1]}{[1 \quad -1 \quad -3 \quad 3 \quad 3 \quad -3 \quad -1 \quad 1]}$	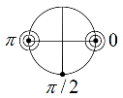
2	$\pi/6$	$\pi/6$	$\frac{[-1 \quad -3 \quad 6 \quad 8 \quad -8 \quad -6 \quad 3 \quad 1]}{[1 \quad -3 \quad -6 \quad 8 \quad 8 \quad -6 \quad -3 \quad 1]}$	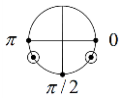
3	$\pi/3$	$\pi/3$	$\frac{[-1 \quad -1-2\sqrt{3} \quad 2\sqrt{3}+6 \quad 4\sqrt{3}+6 \quad -4\sqrt{3}-6 \quad -2\sqrt{3}-6 \quad 1+2\sqrt{3} \quad 1]}{[1 \quad -1-2\sqrt{3} \quad -2\sqrt{3}-6 \quad 4\sqrt{3}+6 \quad 4\sqrt{3}+6 \quad -2\sqrt{3}-6 \quad -1-2\sqrt{3} \quad 1]}$	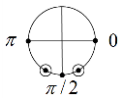
4	$\pi/2$	$\pi/2$	$\frac{[-1 \quad -5 \quad 11 \quad 15 \quad -15 \quad -11 \quad 5 \quad 1]}{[1 \quad -5 \quad -11 \quad 15 \quad 15 \quad -11 \quad -5 \quad 1]}$	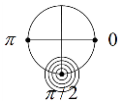
5	$\pi/6$	$\pi/4$	$\frac{[-1, \quad -2-\sqrt{2}, \quad 4+2\sqrt{2}, \quad 5+3\sqrt{2}, \quad -5-3\sqrt{2}, \quad -4-2\sqrt{2}, \quad 2+\sqrt{2}, \quad 1]}{[1, \quad -2-\sqrt{2}, \quad -4-2\sqrt{2}, \quad 5+3\sqrt{2}, \quad 5+3\sqrt{2}, \quad -4-2\sqrt{2}, \quad -2-\sqrt{2}, \quad 1]}$	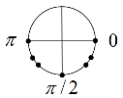
6	$\pi/2$	$\pi/4$	$\frac{[-1 \quad -3-\sqrt{2} \quad 3\sqrt{2}+5 \quad 4\sqrt{2}+7 \quad -4\sqrt{2}-7 \quad -3\sqrt{2}-5 \quad 3+\sqrt{2} \quad 1]}{[1 \quad -3-\sqrt{2} \quad -3\sqrt{2}-5 \quad 4\sqrt{2}+7 \quad 4\sqrt{2}+7 \quad -3\sqrt{2}-5 \quad -3-\sqrt{2} \quad 1]}$	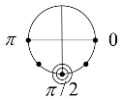
7	$\pi/2$	$\pi/3$	$\frac{[-1 \quad -3-\sqrt{3} \quad 3\sqrt{3}+5 \quad 4\sqrt{3}+7 \quad -4\sqrt{3}-7 \quad -3\sqrt{3}-5 \quad 3+\sqrt{3} \quad 1]}{[1 \quad -3-\sqrt{3} \quad -3\sqrt{3}-5 \quad 4\sqrt{3}+7 \quad 4\sqrt{3}+7 \quad -3\sqrt{3}-5 \quad -3-\sqrt{3} \quad 1]}$	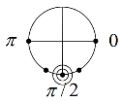
8	$\pi/2$	$\pi/6$	$\frac{[-1 \quad -4 \quad 8 \quad 11 \quad -11 \quad -8 \quad 4 \quad 1]}{[1 \quad -4 \quad -8 \quad 11 \quad 11 \quad -8 \quad -4 \quad 1]}$	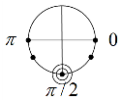
9	$\pi/6$	$\pi/3$	$\frac{[-1, \quad -2-\sqrt{3}, \quad 4+2\sqrt{3}, \quad 5+3\sqrt{3}, \quad -5-3\sqrt{3}, \quad -4-2\sqrt{3} \quad 2+\sqrt{3}, \quad 1]}{[1 \quad -2-\sqrt{3}, \quad -4-2\sqrt{3}, \quad 5+3\sqrt{3}, \quad 5+3\sqrt{3}, \quad -4-2\sqrt{3}, \quad -2-\sqrt{3}, \quad 1]}$	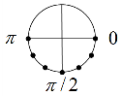
10	0	$\pi/2$	$\frac{[-1 \quad -3 \quad 5 \quad 7 \quad -7 \quad -5 \quad 3 \quad 1]}{[1 \quad -3 \quad -5 \quad 7 \quad 7 \quad -5 \quad -3 \quad 1]}$	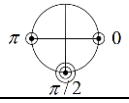

In Table 1, the cut-off frequencies of the filters that involve the use of Eq. (3.19) are shown in columns a and b. The mathematical representation of the filter coefficients (N, D) and its corresponding characteristic diagram according [5] are also shown. To show the robustness of the proposed family of tunable eight-frame filters, in this work we have evaluated several error conditions in order to quantize the existing error.

In optimal conditions, if the system is perfectly tuned at the frequency ω_0, the images or frames recovered from the gathering process are identical to the model above. That is, for the ideal frequency of the filter $\omega = \omega_0$, the estimated phase becomes $\varphi = \phi$. However, in a general case there is a small error (δ), then $\omega = \omega_0 + \delta$ and the estimated phase give us $\varphi = \phi + \Delta\phi$ where, by definition, $\Delta\phi$ is the phase shift detuning error. In other words, the detuning error is the difference between the ideal phase (ϕ) and the estimated phase (φ) and it is quantified as $\Delta\phi = \varphi - \phi$.

Although this error is generally evaluated numerically, in [18] the exact detuning error was obtained from the expression

$$\tan(\Delta\phi) = -\frac{H(\omega + \omega_0)}{H(-\omega - \omega_0)}\sin(2\phi) \tag{3.25}$$

That is, from the known Fourier transform of the filter, we can estimate this kind of miscalibration error. Therefore, for the considerations $\Delta\phi \approx \tan(\Delta\phi)$ and $\sin(2\phi) \approx 1$, the maximum value of this small error becomes,

$$\Delta\phi = -\frac{H(\omega + \omega_0)}{H(-\omega - \omega_0)} \tag{3.26}$$

Using the considerations $\omega_0 = \pi / 2$ and $\delta = \omega - \omega_0$ into Eq. (3.19) and after some algebra, the detuning expression is given by

$$\Delta\phi = -\tan\frac{\delta}{2}\left[\frac{\cos(\delta) - \sin(a)}{\cos(\delta) + \sin(a)}\right]\left[\frac{\cos(\delta) - \sin(b)}{\cos(\delta) + \sin(b)}\right] \tag{3.27}$$

By using the last equation, the expressions describing the detuning function of each one of the novel filters in Table 1 were generated. This was achieved by evaluating each of the cut-off frequencies a and b. To illustrate some examples, for the particular case $b = a$ (examples 1, 2, 3 and 4 described in Table 1) the detuning error reduces as

$$\Delta\phi = -\tan\frac{\delta}{2}\left[\frac{\cos(\delta)-\sin(a)}{\cos(\delta)+\sin(a)}\right]^2 \tag{3.28}$$

So for the particular cut-off frequency $a = b = \pi/2$ from Table 1, we obtain

$$\Delta\phi = \tan\left(\frac{\delta}{2}\right)\left[\frac{\cos(\delta)-1}{\cos(\delta)+1}\right]^2 = \tan\left(\frac{\delta}{2}\right)\left[\frac{-2\sin^2(\delta/2)}{2\cos^2(\delta/2)}\right]^2 = -\tan^5\left(\frac{\delta}{2}\right) \tag{3.29}$$

Therefore, this filter is exceptionally good to compensate the detuning errors with a phase step $\omega_0 = \pi/2$

In the same way, from Eq. (3.27) the detuning error for the filter No. 10 in Table 1 becomes,

$$\Delta\phi = -\tan\frac{\delta}{2}\left[\frac{\cos(\delta)-\sin(0)}{\cos(\delta)+\sin(0)}\right]\left[\frac{\cos(\delta)-\sin(\pi/2)}{\cos(\delta)+\sin(\pi/2)}\right] = -\tan\frac{\delta}{2}\left[\frac{\cos(\delta)-1}{\cos(\delta)+1}\right] = \tan^3\frac{\delta}{2} \tag{3.30}$$

The filter above exhibits a linear insensitivity to the bias error because it has a double root at zero ($H'(0) = 0$) [19]. Thus, this filter is exceptionally good since it corrects bias and detuning errors simultaneously. For the particular case $a = b = \pi/3$ (example 3 in Table 1)

$$\Delta\phi = -\tan\frac{\delta}{2}\left[\frac{\cos(\delta)-\sin(\pi/3)}{\cos(\delta)+\sin(\pi/3)}\right]^2 = -\tan\frac{\delta}{2}\left[\frac{2\cos(\delta)-\sqrt{3}}{2\cos(\delta)+\sqrt{3}}\right]^2 \tag{3.31}$$

This is a filter with a flat bandwidth response and a maximum error of the phase on the order of $4\text{x}10^{-4}$ between a frequency range of $\pi/3$ to $2\pi/3$ (60° and 120°), as shown in Fig. 3.1. Finally, it should be noticed that for the particular case $a = b = 0$ (example 1 showed in Table 1)

$$\Delta\phi = -\tan\frac{\delta}{2}\left[\frac{\cos(\delta)-\sin(0)}{\cos(\delta)+\sin(0)}\right] = -\tan\frac{\delta}{2} \tag{3.32}$$

This is the well-known behavior of the detuning error of a three-step filter and it is depicted in Fig. 3.1. This explains why the traditional three and some four-step filters are very sensitive to the detuning error, and the experiments for using them require very little vibration and a small amount of miscalibration errors. Hence the importance of this type of eight-step filters, which

despite requiring many more steps than conventional ones, need not be so perfect in order to simultaneously correct various types of errors. This means that an experiment can be much simpler and cheaper; for example, with the use of a simple FPP arrangement, using a conventional CCD camera, a common multimedia projector and an ambient illumination of fluorescent light, we achieved accuracies of the order of 10^{-6} m, by measuring the topography of samples of small size [21]. To depict the behaviors of the detuning errors of the filters obtained in Table 1, we plotted the response of the detuning in two figures, divided in filters with a broadband and the filters with high compensation for the phase shifting detuning error.

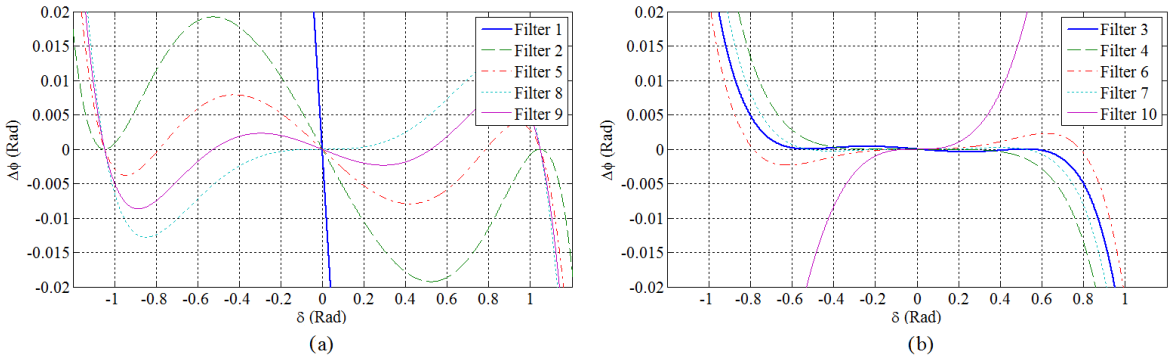

Fig. 3.1: Detuning of the filters present in Table 1. (a) Mostly broadband filters. (b) Best compensate the detuning error.

The filter 3 of Fig. 1(a) is the most balanced because it is a broadband filter and it corrects the bias and detuning errors. The filter corresponding to $a = b = \pi / 2$ from Table 1 is the most balanced to minimize the detuning error of most of the cases with considerable error of this type. The magnitude of the detuning error ($\Delta\varphi$) is widely used to evaluate the robustness of the detuning error of the TPS algorithms and generally it is evaluated numerically. Using the same data of Fig. 3, we can generalize the detuning responses in phase filters as shown in Fig 3.2.

Whereas, we were able to calculate exact analytical expression, a graphical representation of the detuning error is shown in Fig. 3.1

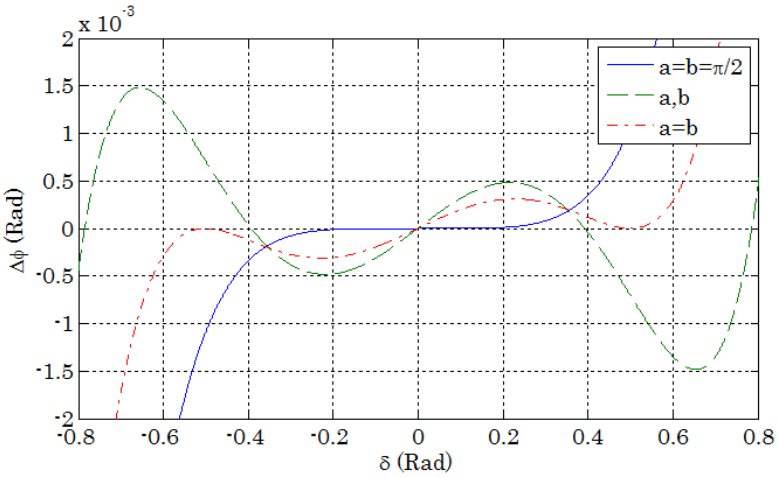

Fig. 3.2: Plot of the phase shift detuning error.

By applying the proposed method, we obtain several results. First, in Fig. 3.1, blue-solid line is the $\pi/2$ response that best satisfies the requirements of the experiment. Depicted green-dashed line is a symmetric response, cancels $\pi/2$, a and b frequencies and moreover, it is a wide bandwidth filter. Finally, depicted red (dash-dot) line is the quadratic response for the phase shift detuning error.

The robustness of the proposed family of tunable eight-frame filters is shown in Fig 3.3, were the absolute normalized response of the filters is simulated in several profiles in order to quantize the existing error. In Fig. 3.2 are shown the simulated responses of the filters obtained with the two-frame filter formalism. The detuning error of the differences among most of the reconstructed phases is of the order of 0.01%.

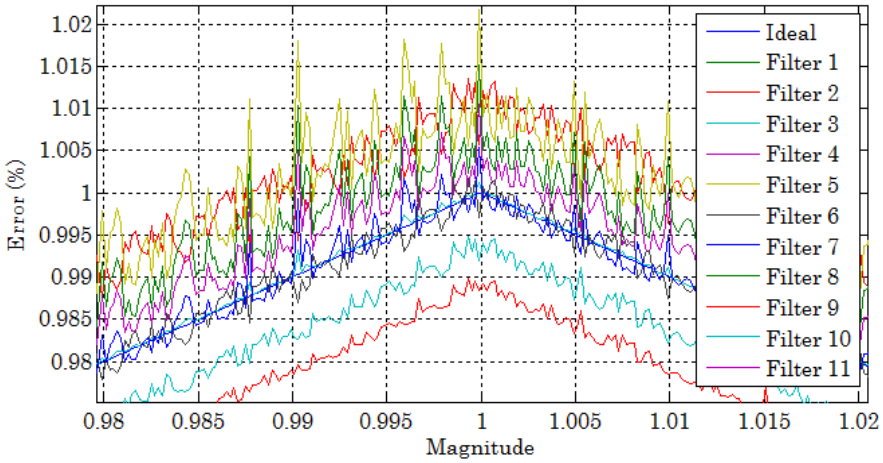

Fig. 3.3: Numerical simulation of the response (normalized) of the proposed filters.

Then, by simulating a 3D profile, we vary the amount of random detuning and bias error on each of the eight temporal phases simulated. Some selected reconstructed functions are shown in Fig. 3.4.

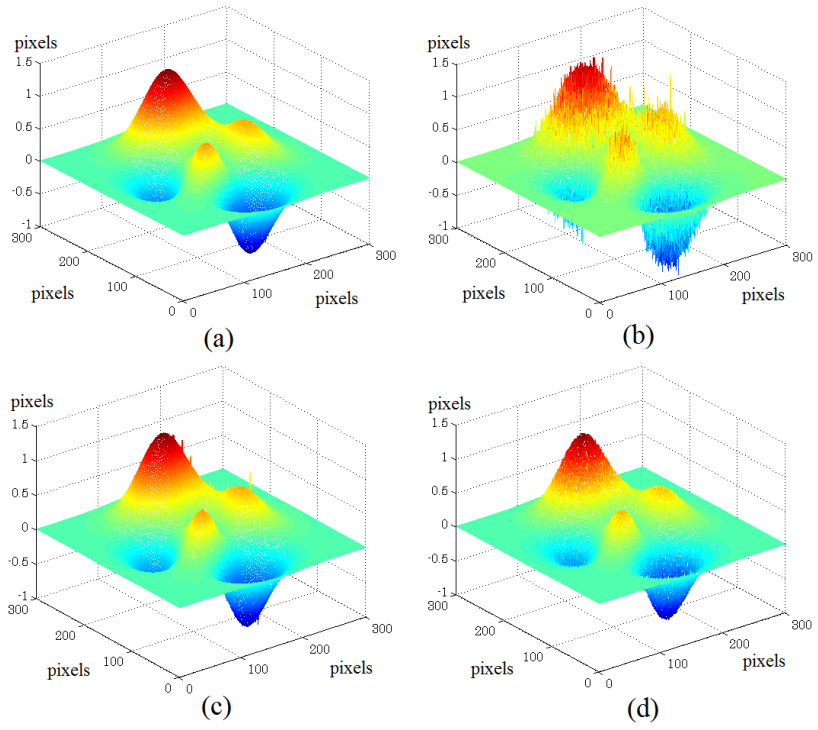

Fig. 3.4: Function simulated with special cases of the filters applying random noise of 20% in bias and detuning errors.

The set of eight-frame filters are exceptionally good to recover the wrapped phase when miscalibration errors are present. Ideal function [Fig. 3.4(a)] is depicted to compare results. Fig 3.4(b) shows a least-squares filter, meanwhile in Figs. 3.4(c) and 3.4(d) the responses of filters 2 and 10 proposed in Table 3.1 are depicted, both attain a satisfactory recovery and without distortion. (To show the wideband response we choose the filter No. 2 tuned at $\pi/6$).

3.3 Response of the proposed filters

In order to evaluate the robustness of the proposed filters, we used a profile simulation to quantify the error of those filters and compared such results. Fig. 3.5 shows the simulated responses of the eight-frame filters obtained with the two-frame formalism with an added random noise (different at each point of the plots) of 15% of the original signal.

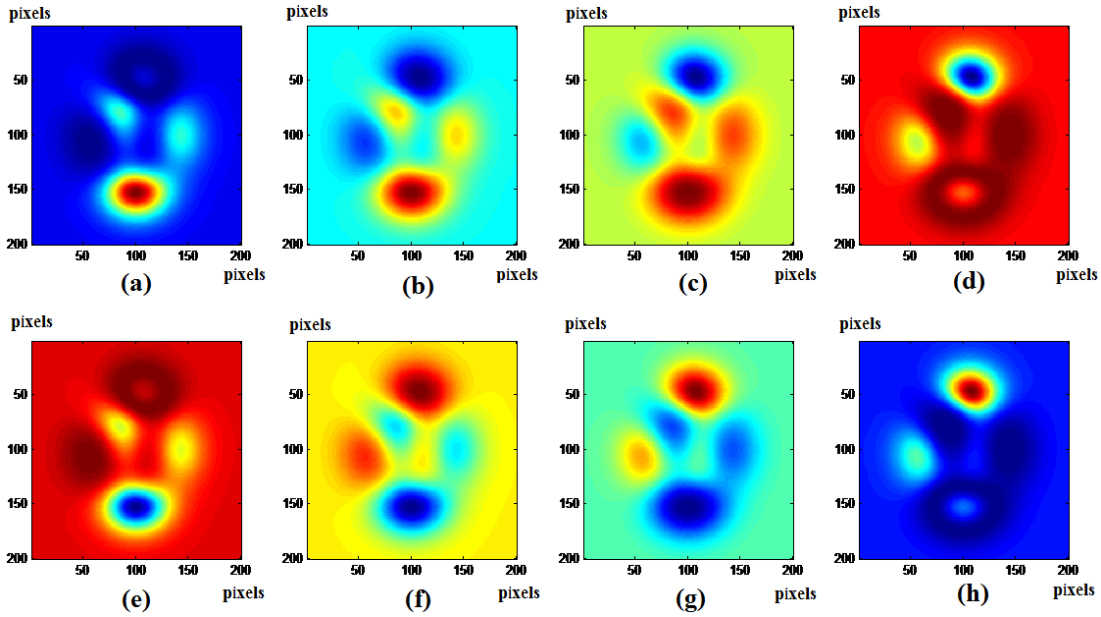

Fig. 3.5: Eight numerical phases simulated for the response of the proposed set of filters showed in Table 1 with random additive noise. Steps are: (a) π/4, (b) π/2, (c) 3π/4, (d) π, (e) 5π/4, (f) 3π/2, (g) 7π/4, and (h) 2π.

The estimated phase error of the differences among most of the reconstructed phases of Fig. 3.5 is of the order of 0.02%. However, by simulating a 3D profile, we observed the response of the filters to a surface function. In this case, we use the function “peaks” of the MATLAB software and randomly varied the amount of detuning at each pixel of each of the eight temporal phases simulated; then we obtained the phase with the use of the designed eight-frame filters and finally we retrieved the surface. Selected reconstructed functions (normalized) of the algorithms of Table 1 are shown in Fig. 3.6.

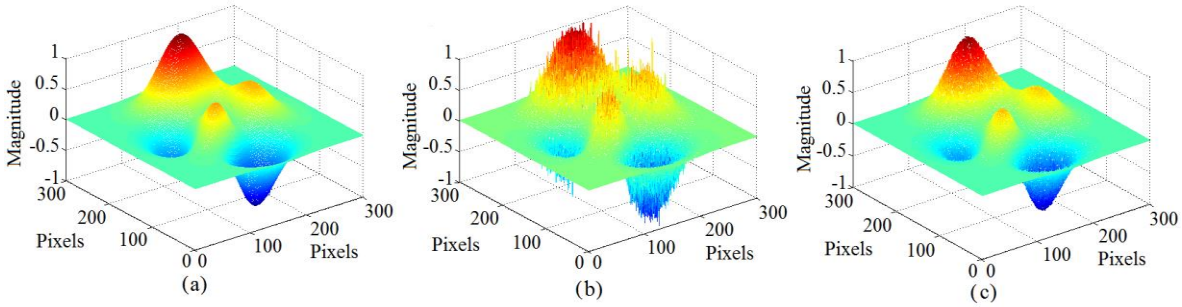

Fig. 3.6: Functions simulated for some special cases of the filters applying 20% of random additive noise.

The set of eight-frame filters is exceptionally good to recover the wrapped phase when miscalibration errors are present. The ideal function (Fig. 3.6(a)) is depicted to compare the results. Fig. 3.6(b) shows a least-square filter; meanwhile in figure 3.6(c) the response of filter No. 10 in Table 1 is depicted to show the wideband response of the filter. From figure 3.6, we can observe that filter No. 10 attains a satisfactory recovery of the shape without distortion. The importance and usefulness of these eight-frames filters is that with these analytical expressions, we can compensate bias and detuning errors in first, second, and even third order (by selecting the appropriate cut-off frequencies). Moreover, this formalism makes it possible to obtain the exact expression of the detuning at which the filter can be designed, based on the desired

detuning. Similarly, it occurs with the bias error. The filters are versatile and they correct a large amount of experimental errors. Finally, due to the fact that the conditions under the experimental data taken are different for each experiment, each type of error is compensated by a different filter.

In summary, this is a completely novel family of symmetrical tunable eight-frame TPS filters for use in phase-shifting interferometry (PSI) or in a PSP system. These filters were obtained by the two-frame algorithm. Particular cases are shown in Table 1. The Fourier and detuning responses for some particular cases are depicted as proof of the tunable wideband response. That is, the filters are robust against the most common miscalibration errors such as phase shifting detuning and bias. Finally, some cases of simulated errors showed that the family of filters proposed in this work is immune to miscalibration random errors for about 20% of the real value simulated, varying only 0.001% of the original signal under study.

3.4 Proposal of eight-frame phase shifting algorithms for semi-fossilized materials

Although the literature shows several TPS algorithms to recover the wrapped phase with eight-frames, the amount of eight-frame filters is limited to one very specific carrier frequency. While the Carré algorithm has been proved as the only self-tunable filter [22], and due to the fact that it fails when there is more than one cut-off frequency, for the specific step $\pi/4$, only the least-square estimation is available owing to its tolerance to harmonics. The other eight-frame algorithm approaches are tuned in other steps or cut-off frequencies ($\pi/2, \pi/3$, etc.). Therefore, a filter insensitive to linear bias, to detuning, and tuned at the desired cut-off

frequencies is very useful. To design this filter, a novel solution that consists of an eight-step filter capable of tuning on two or more arbitrary frequencies and that can be designed in a simple manner is presented in this work. This filter has up to seven parameters, one of them necessarily cuts off the fundamental frequency and another cuts off the DC component, and the five remaining parameters can be utilized to select the manner in which we want to achieve immunity to quadratic or cubic detuning and bias errors, the linearity and other types of errors as well [5,19]. Additionally, the expression of the maximum detuning for an eight-frame filter is obtained (Eq. (3.26)) in an analytical and accurate manner, which allows us to design and carefully select the detuning error in which the filter will be immune.

By modeling the fringes with the equation shown in Eq. (3.5), the PSP problem is usually reduced to four steps:

I. *M* images are captured with several phase shifting among them.
II. To choose or design a specific M-frames phase shifting algorithm (PSA) to process the set of M images to obtain the wrapped phase.
III. An unwrapping algorithm to recover the desired phase is designed.
IV. A texture is applied to the obtained phase to exhibit the desired target.

In the first step, a set of eight fringe frames (intensity patterns) are acquired from an experimental set up. For the second step, several algorithms have been developed to calculate the phase of a fringe pattern; however, some of them, so called PSA, simply use intensity values obtained by shifting the phase of the intensity pattern to calculate the phase [23]. Thus, developing algorithms sufficiently robust and immune to most of the common experimental errors has been based on the objective of comparing most of the main algorithms [24]. On the other hand, many algorithms have not been specifically used for experiments using real data. The spatial non uniformity of the phase shift is also an important problem in applying phase-

shifting techniques in FPP systems, because of the variation of fringe visibility along the optical path. This is mathematically equivalent to the variation of phase-shift errors (depending on the position), problem that is out of the scope of this work [25]. The main goal of this thesis is to calculate several algorithms to recover efficiently the profile and with the quality requirements needed for small targets of biological material. In the same way, these filters must exhibit the adequate properties to compensate for some of the common errors present in practical applications.

It should be highlighted that an eight-frame algorithm corresponds to a filter with seven independent parameters to recover the desired phase and to compensate for some errors. Then, at least two of those parameters are necessary to eliminate the D.C. component and the fundamental frequency. Two additional conditions are used to compensate the linear bias variation and the linear phase shift detuning error [8]. The remaining three conditions are used to compensate for other errors generated by other effects, like a non-linearity response, and to obtain a better SNR. After testing well-known filters of three, four, five, six, seven and more steps, we concluded that by using seven or more frames the resolution obtained was in the parameters required for this type of target. The response did not improve substantially when using nine or more frames. However, when analyzing the histogram of the estimated frequency of tuning, the Hibino filter had the best response closer to the one expected (due its broadband and tuned on $\pi/4$).

However, this filter was not designed for the conditions of our experiment [26], thus for that reason we generated a robust filter range, designed specifically for the needs of our experiment: a broadband filter, tuned on $\pi/4$, insensible to bias variations and detuning errors, (specially linear) and, a good SNR.

The estimated phase of any quadrature filter with an M-th order is given by Eq. (3.10) [5, 6, 8, 20], and again, it should be noted that $\vec{\mathbf{I}} = \begin{bmatrix} I_1 & I_2 & \dots & I_M \end{bmatrix}^T$ is the column vector of

frames, and *N* and *D* are the desired numerator and denominator row vectors. According to references 8, 19, and 20, the Fourier transform $H(\omega)$ of this filter is,

$$H(\omega) = (-2)^M \prod_{k=1}^{M} \sin\left[(\omega - \alpha_k)/2\right] \tag{3.33}$$

where each α_k is the cut off frequency or zero of the Fourier impulse response of the filter. In other words, the design of a filter becomes a geometrical problem, and it is reduced to choose a set of *M-1* frequencies that are the necessary conditions to be a specific filter [8, 20]. Therefore, from Eq. 3.10, the general case for *M*=8, the corresponding eight-frame algorithm is,

$$\tan(\varphi) = \frac{N\vec{\mathbf{I}}}{D\vec{\mathbf{I}}} = \frac{b_1 I_1 + b_2 I_2 + b_3 I_3 + b_4 I_4 + b_5 I_5 + b_6 I_6 + b_7 I_7 + b_8 I_8}{a_1 I_1 + a_2 I_2 + a_3 I_3 + a_4 I_4 + a_5 I_5 + a_6 I_6 + a_7 I_7 + a_8 I_8} \tag{3.34}$$

Then, an option to obtain the required ratio *N/D* with symmetric coefficients is obtained from the expression in Eq. (3.11). For M=8 the result is shown in Eq. (3.12). Assuming that the phase step is $\pi/4$, it is well known that a filter that eliminates harmonics corresponds to the cut-off frequencies $\alpha_k = 0$, $\pi/4$, $\pi/2$, $3\pi/4$, π, $5\pi/4$ and $3\pi/2$ [8, 19, 20, 27]. That is, to be a quadrature filter, the two necessary cut off frequencies are zero and the phase step $\pi/4$ [19]. However, in a least-squares procedure the harmonics are also eliminated. Therefore, from Eq. (3.15) and after solving some algebra operations the obtained eight-frame algorithm is,

$$\tan(\varphi) = \frac{\left[-1,\ -1-\sqrt{2},\ -1-\sqrt{2},\ -1,\ 1,\ 1+\sqrt{2},\ 1+\sqrt{2},\ 1\right]\vec{\mathbf{I}}}{\left[1+\sqrt{2},\ 1,\ -1,\ -1-\sqrt{2},\ -1-\sqrt{2},\ -1,\ 1,\ 1+\sqrt{2}\right]\vec{\mathbf{I}}} \tag{3.35}$$

Additionally, in [8, 20], it is demonstrated that, from an individual algorithm an infinite number of equivalent phase shifted algorithms can be obtained. However, for the particular case, where each individual two-frame filter is phase shifted by an angle of $\theta_k = \alpha_k/2$, the corresponding phase shifted filter N_r/D_r from Eq. (3.11) becomes,

$$\frac{N_r}{D_r} = \underset{k=1}{\overset{M-1}{\Omega}} \left\{ \frac{\left[\cos\alpha_k,\ -1\right]}{\left[\sin\alpha_k,\ 0\right]} \right\} \tag{3.36}$$

Then, for *M=8*, the result equivalent to Eq. (3.12) becomes,

$$\frac{N_r}{D_r} = \prod_{k=1}^{7} \left\{ \frac{\left[\cos\alpha_k, \quad -1\right]}{\left[\sin\alpha_k, \quad 0\right]} \right\} \tag{3.37}$$

And the equivalent phase shifted filter is,

$$\tan(\varphi) = \frac{\left[-\sqrt{2}, \quad -2, \quad -\sqrt{2}, \quad 0, \quad \sqrt{2}, \quad 2, \quad \sqrt{2}, \quad 0\right]\vec{\mathbf{I}}}{\left[-\sqrt{2}, \quad 0, \quad \sqrt{2}, \quad 2, \quad \sqrt{2}, \quad 0, \quad -\sqrt{2}, \quad -2\right]\vec{\mathbf{I}}} \tag{3.38}$$

This case is equivalent to the well-known least-squares filter that can be used for this application with certain restrictions, because it is sensible to bias and detuning errors. On the other hand, for the analysis of an eight frame series of interferograms we can use auto tuning methods like the Carré's algorithm, or the algorithm with immunity to systematic errors, as the Surrel technique based on (N+1) bucket [5, 27] and others [28-30]. However, these filters are not based on the analysis inside the physical phenomena involved in the experiment and they do not make a tuning in the best step observed with an error estimator of the obtained phase in the experimental data. Hence, the need of implementing an algorithm and a phase filter according the experimental data. To develop this algorithm, we use the two-frame filter method previously reported [8], considering α as the ideal phase step to tune the filter, then a new (n + m-1) frame filter is obtained from two individual filters as shown in Eq. (3.33). As mentioned before, the design of a tunable filter allows this case to be extended further to an eight-frame filter, which allows the selection of the data to be removed. Furthermore, we select polynomial roots implying that the filter must suppress frequencies in Fig. 3.7. To assure that the filter eliminates harmonics, undesirable frequencies and the systematic errors involved, we first propose a filter to deal with harmonics, mainly as in Eq. (3.37). Also, we define a filter that is able to handle an optimal SNR and linear detuning errors as *0*, $\pi/4$, $\pi/4$, $\pi/2$, $3\pi/4$, $3\pi/4$, π (from now known as mainly detuning error filter or MDE filter). Applying the same method to design a filter that compensates mainly bias errors (MBE filter) associated to the system, we calculate a

filter considering cut off frequencies in *0, 0,* $\pi/4$, $\pi/2$, $3\pi/4$, π, π, and finally a filter centered in *0, 0,* $\pi/4$, $\pi/4$, $\pi/2$, $3\pi/4$, π to compensate detuning and bias errors (DBE filter). Graphic representation of these filters with their cut off frequencies is shown in Fig. 3.7 according to [5].

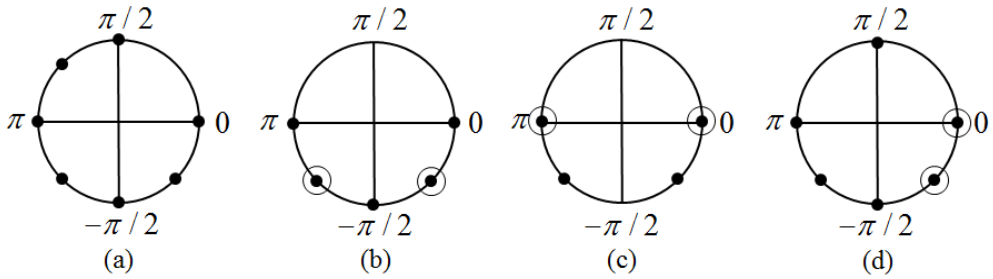

Fig. 3.7: Plot of the polynomial characteristic of an harmonics suppress filter (a), an insensible to linear detuning filter (b), a mainly bias error filter (c) and a detuning + bias compensating filter (d). All were obtained with the two-frame filter method.

Then, applying the above procedure for the rest of the filters shown in Fig. 3.7, from Eq. (3.11) the filter shown in Fig. 3.7(b) is,

$$\tan(\varphi)=\frac{\left[-1,\ \ -1-2\sqrt{2},\ \ 5+2\sqrt{2},\ \ 5+4\sqrt{2},\ \ -5-4\sqrt{2},\ \ -5-2\sqrt{2},\ \ 1+2\sqrt{2},\ \ 1\right]\vec{\mathbf{I}}}{\left[1,\ \ -1-2\sqrt{2},\ \ -5-2\sqrt{2},\ \ 5+4\sqrt{2},\ \ 5+4\sqrt{2},\ \ -5-2\sqrt{2},\ \ -1-2\sqrt{2},\ \ 1\right]\vec{\mathbf{I}}} \tag{3.38}$$

And from Eq. (3.37) the equivalent algorithm is,

$$\tan(\varphi)=\frac{\left[0,\ \ -1-2\sqrt{2},\ \ 0,\ \ 4\sqrt{2}+5,\ \ 0,\ \ -5-2\sqrt{2},\ \ 0,\ \ 1\right]\vec{\mathbf{I}}}{\left[1,\ \ 0,\ \ -5-2\sqrt{2},\ \ 0,\ \ 4\sqrt{2}+5,\ \ 0,\ \ -1-2\sqrt{2},\ \ 0\right]\vec{\mathbf{I}}} \tag{3.39}$$

In the same manner, the filter shown in Fig. 3.7(c) gives us the expressions,

$$\tan(\varphi)=\frac{\left[-1,\ \ -1-\sqrt{2},\ \ 3+\sqrt{2},\ \ 3+2\sqrt{2},\ \ -3-2\sqrt{2},\ \ -3-\sqrt{2},\ \ 1+\sqrt{2},\ \ 1\right]\vec{\mathbf{I}}}{\left[1,\ \ -1-\sqrt{2},\ \ -3-\sqrt{2},\ \ 3+2\sqrt{2},\ \ 3+2\sqrt{2},\ \ -3-\sqrt{2},\ \ -1-\sqrt{2},\ \ 1\right]\vec{\mathbf{I}}} \tag{3.40}$$

and the corresponding equivalent algorithm is

$$\tan(\varphi)=\frac{\left[0,\ \ -1-\sqrt{2},\ \ 0,\ \ 3+2\sqrt{2},\ \ 0,\ \ -3-\sqrt{2},\ \ 0,\ \ 1\right]\vec{\mathbf{I}}}{\left[1,\ \ 0,\ \ -3-\sqrt{2},\ \ 0,\ \ 3+2\sqrt{2},\ \ 0,\ \ -1-\sqrt{2},\ \ 0\right]\vec{\mathbf{I}}} \tag{3.41}$$

Finally, the last case showed in Fig. 3.7(d) gives us the algorithms,

$$\tan(\varphi)=\frac{\left[-1,\ \ 5+3\sqrt{2},\ \ -3\sqrt{2}-3,\ \ -9-6\sqrt{2},\ \ 9+6\sqrt{2},\ \ 3\sqrt{2}+3,\ \ -3\sqrt{2}-5,\ \ 1\right]\vec{\mathbf{I}}}{\left[-1-\sqrt{2},\ \ 1,\ \ 6\sqrt{2}+7,\ \ -7-5\sqrt{2},\ \ -7-5\sqrt{2},\ \ 6\sqrt{2}+7,\ \ 1,\ \ -1-\sqrt{2}\right]\vec{\mathbf{I}}} \tag{3.42}$$

and

$$\tan(\varphi)=\frac{\left[1,\ \ -2-2\sqrt{2},\ \ -1+\sqrt{2},\ \ 6+4\sqrt{2},\ \ -3-2\sqrt{2},\ \ -4-2\sqrt{2},\ \ 3+\sqrt{2},\ \ 0\right]\vec{\mathbf{I}}}{\left[-1,\ \ -\sqrt{2},\ \ 5+3\sqrt{2},\ \ -2-\sqrt{2},\ \ -5-4\sqrt{2},\ \ 2+3\sqrt{2},\ \ 1+\sqrt{2},\ \ -\sqrt{2}\right]\vec{\mathbf{I}}} \tag{3.43}$$

Then, from Eq. (3.33), the Fourier response of each filter is easily obtained, and the results are depicted normalized in Fig. 3.8.

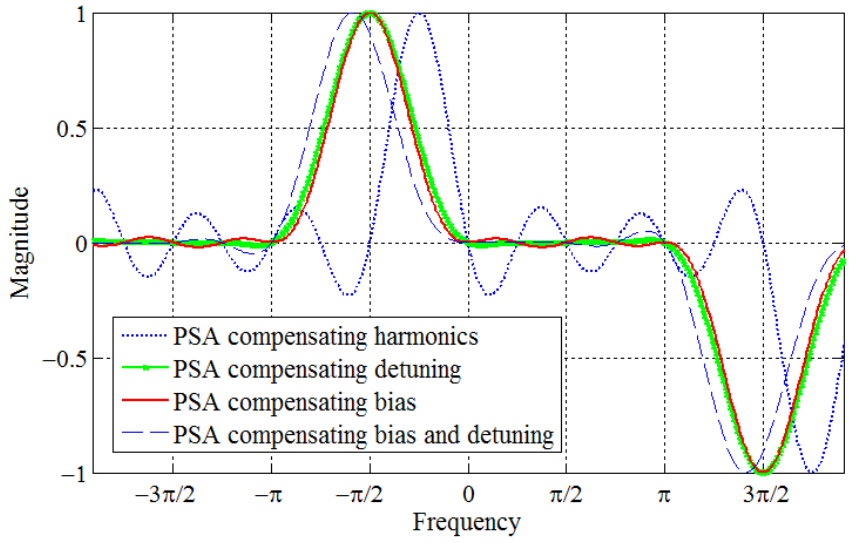

Fig. 3.8: Normalized Fourier response of the four algorithms calculated with two-frame algorithm method.

Notice than the obtained filters above satisfied a wide range of requirements for any experiment. That is, considering that the ideal quadrature filter is a step function, the ratio of the area under the curve between the right and the left side of the graphic, starting from zero, gives us an idea of how the filter works, and why the best approximation for this application is depicted as the green line corresponding to a PSA compensating detuning or MDE. Additionally, we can observe the response for the phase shift detuning, bias, and harmonics (Fig. 3.9).

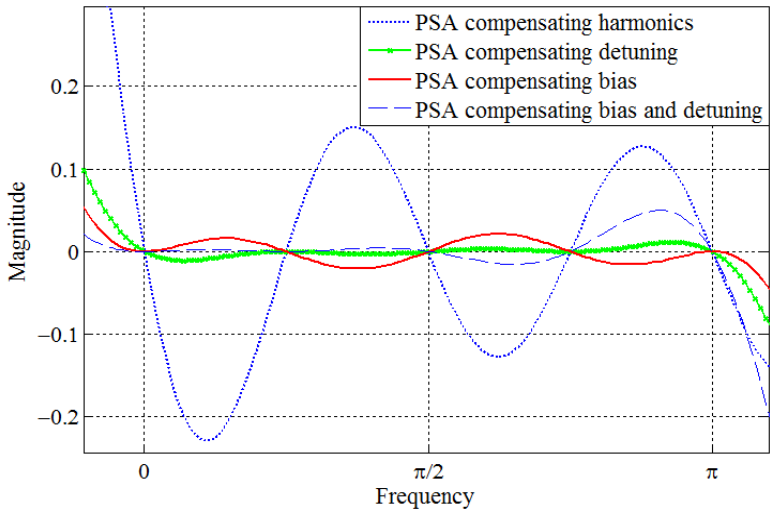

Fig. 3.9: Normalized response of the filters proposed to detuning error, bias error and harmonics.

This graph verifies the design of the filters MBE and DBE, having a double cutoff frequency at zero and therefore it is sufficient to compensate the bias error. In the same way, the green trace (or MDE filter) in the tuning frequency $\pi/4$ has a similar response and this makes it insensitive to linear detuning error. Furthermore, linearity is given by the symmetry of the function in $\pi/2$ and the filter with the lowest area under the curve has better SNR. Since each filter is defined to counteract a specific error, we cannot choose one of the algorithms as the best for a given

application. Indeed, all proposed filters are good and efficient to compensate for the error by which they were designed. The phase shift detuning error is depicted in Fig. 3.10.

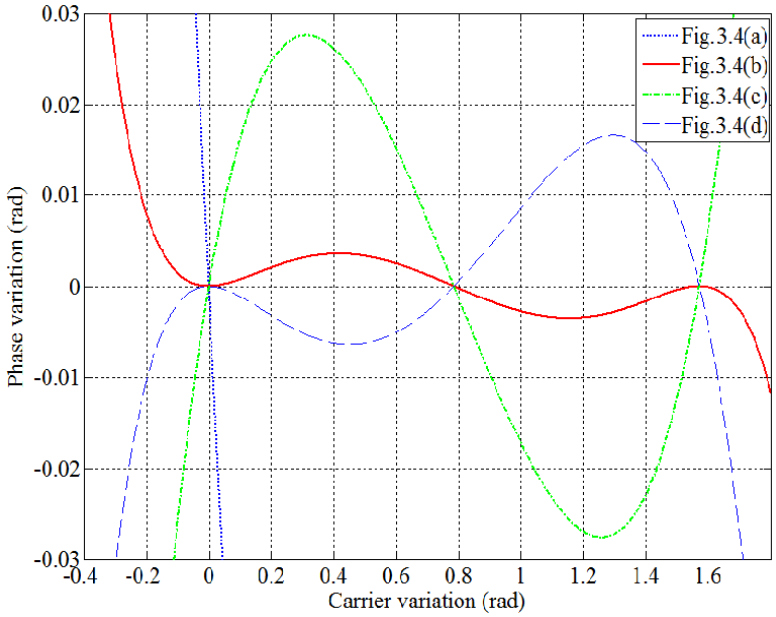

Fig. 3.10: Phase shift detuning error of the filters in Fig. 3.7.

As expected, when the difference between the ideal and the observed carrier is zero, the phase error is zero. Having a carrier variation between -0.2 and 1.6 rad, the estimated phase error is less than 0.03 rad. This implies that the filters in Figs. 3.7(b) and 3.7(d) are broadband filters, where the best performance is from the filters MDE (Fig. 3.7(b)) and BDE (Fig. 3.7(d)).

3.5 Evaluation of the proposed algorithms

Among all the algorithms analyzed, the MBE filter is the one that best meets the requirements of an experimental optical set up, by providing a good response to detuning, an acceptable

tolerance to harmonics and a real attenuation of systematic errors. The Fourier response of the MBE filter and its detuning error are depicted in Fig. 3.11.

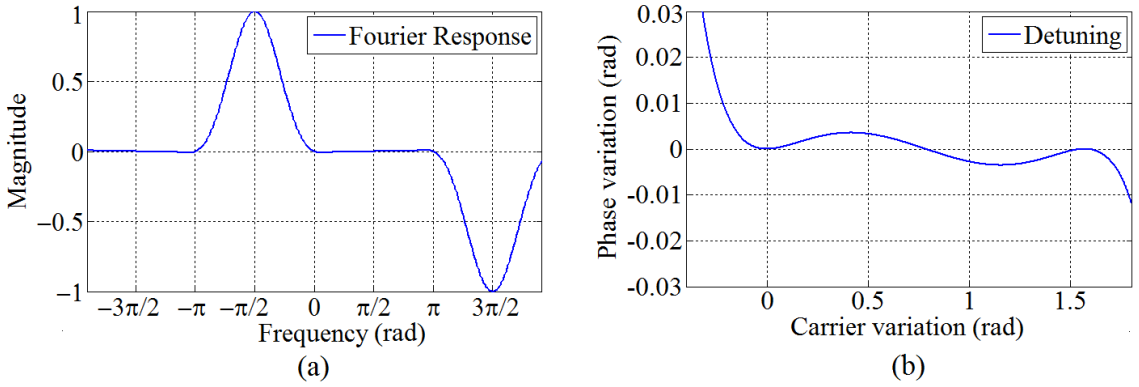

Fig. 3.11: (a) Normalized Fourier response of the algorithm calculated with the two-frame method. (b) Phase shift detuning error of the filter.

In order to evaluate the robustness of the proposed filters, we use a simulation of a profile to quantify the error of those filters and to compare such results with a single four-frame filter and a Hibino filter (such comparisons were made among Surrel [27], Hibino [25] and de Groot [3] filters; however, the Hibino filter shows a better curve fitting with the parameters included in these simulations). First, we simulate a profile by using the Eq. (3.1). Random noise is then added as detuning error in the form of $\omega = \omega + \Delta\omega$ and bias error as $b = b + \Delta b$ to the fringe pattern. Increasing the detuning error until a 10% and the bias error until a 20%, we started to see the different trends of each of the filters as shown in Fig. 3.12.

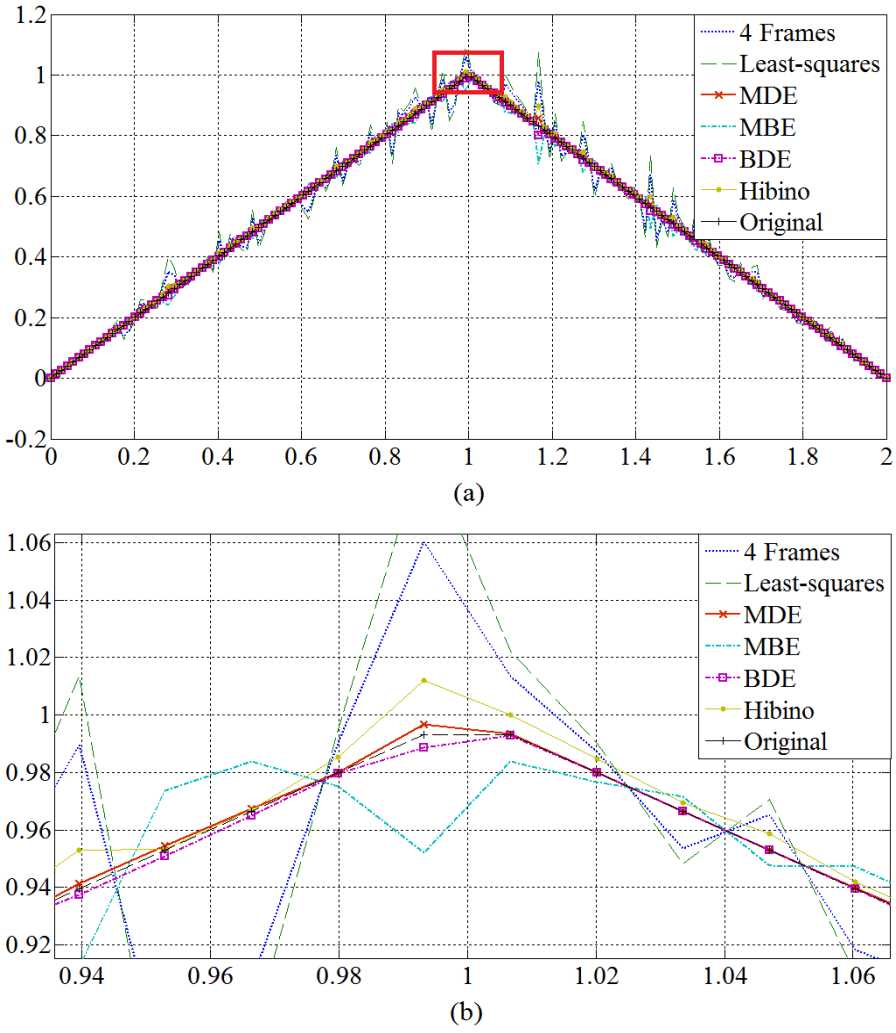

Fig. 3.12: (a) Simulation of algorithms and their errors. (b) Detailed view of the red square region in (a).

The best filter observed, the MDE filter, has an error average of 0.2% and an average of deviation of errors of 0.4%. Note that with random detuning and bias errors, these results are inconclusive for a filter that is capable of removing a broadband of unwanted frequencies. As one of the best and most used phase shifting filters, the 4-step filter appears just for comparison purposes. Table 3.2 shows the average of errors and deviations of this simulation.

Table 3.2: Error present in the filters.

Filter	Average	Deviation
4-step	0.0038739	0.0846345
Least-squares	0.0018890	0.1206078
MDE	0.0020027	0.0046684
MBE	0.0058631	0.0378228
BDE	0.0027184	0.0058538
Hibino	0.0110755	0.0141697

From Table 3.2 we can notice that the function that has a lower error rate is, as expected, the least-squares filter, this is because the function is designed to precisely obtain the least square error of the simulated points. Nonetheless, the MDE filter has better performance with less error because despite having a slightly higher average error than the least-squares filter, in the deviation of data, we can observe that it is much higher than the least-square filter. In the same manner, now we simulate a more complex function, as the well-known peak function from the MATLAB, as shown in Fig. 3.13. In this case we use a 15% of bias and 10% of detuning randomly added to the original plot.

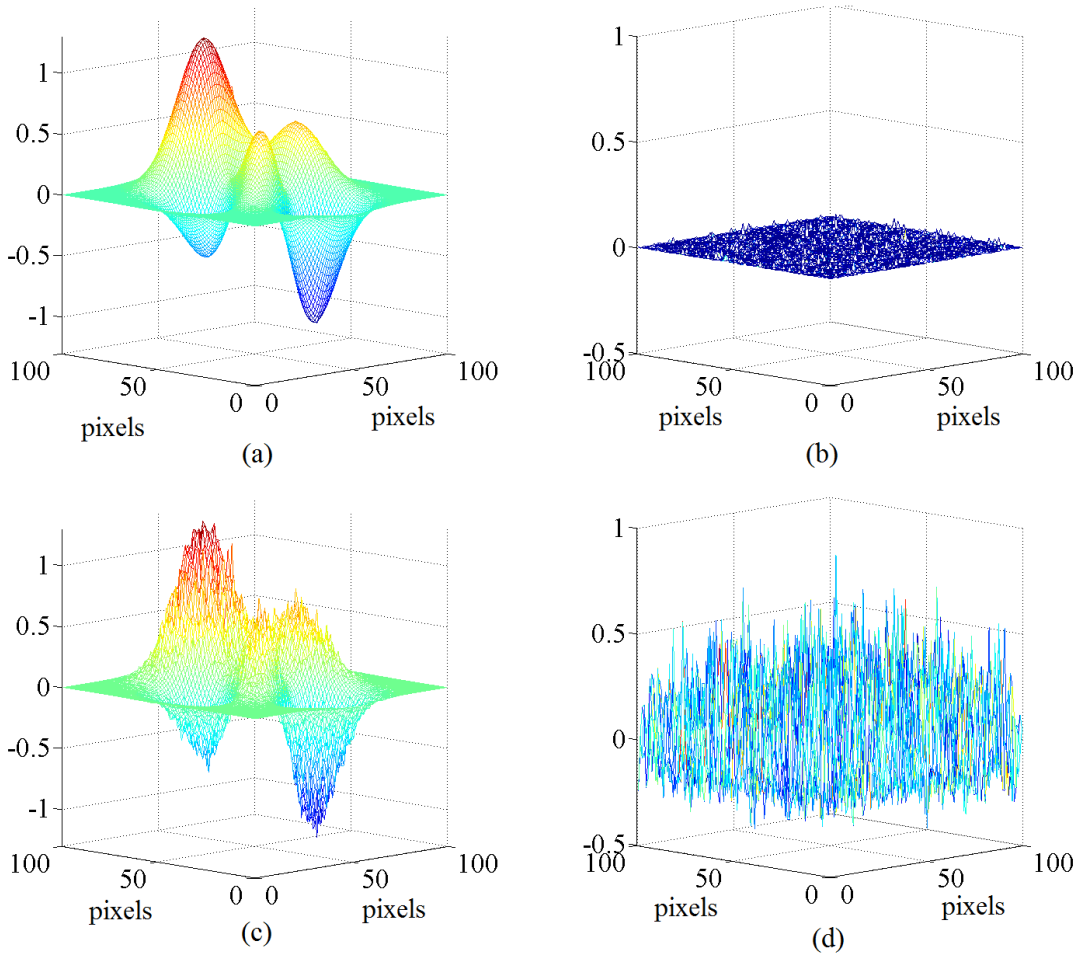

Fig. 3.13: Simulated reconstruction of the normalized "peaks" function with the (a) MDE filter and the (b) Least-squares filter. Average errors are shown in (b) and (d) respectively.

A statistical study for each of the filters used is carried out in order to evaluate the quality of each one in the presence of random noise. This study is based in the Pearson's correlation coefficient, which is an index that measures the linear relationship between two random variables quantitative. The Pearson's correlation coefficient between two variables is defined as the covariance of the two variables divided by the product of their standard deviations. The form of the definition involves a "product moment", that is, the mean (the first moment about the

origin) of the product of the mean-adjusted random variables. Then, to obtain the standard deviation and average error indicators, first we subtract the graphic obtained with random errors from the ideal graphic without errors, followed by an average of all the points to finally obtain the average error of that filter in the simulation. For deviation, initially we have to get the standard deviation of all the points to then average them. Table 3.3 shows the results obtained. The closer the correlation coefficient is to one, the more it resembles the original function.

Table 3.3: Errors of the filters according the simulation of the "peaks" function.

Filter	Average	Deviation	Correlation coefficient
4-step	-0.0046	0.0952	0.994520
Least-squares	-0.0162	0.1411	0.988480
MDE	-0.0023	0.0044	0.999985
MBE	0.0087	0.0424	0.998860
DBE	0.0030	0.0054	0.999978
Hibino	-0.0138	0.0161	0.999839

From Table 3.3, it is observed that the lesser average error corresponds to the MDE filter; however, a four-step filter was better than MBE filter due to the fact that while the more steps are acquired, the error introduced in the algorithm for obtaining the wrapped phase also increases. From the simulations, we can conclude that for cases where detuning errors or bias errors are present, the proposed filters, tuned on $\pi/4$, are sufficient to retrieve accurate information of an object despite a great variety of experimental random noises. Finally, from the Pearson's coefficient, we obtain the correlation between the original sample and the estimated phase, and as we expect the filters MDE and MBE were the best choices again.

3.6 MBE phase filter for semi-fossilized samples

A set of eight images of a semi-fossilized sample were digitalized using a FPP system, and then processed to analyze the quality of the topography considering the level of quality required for palaeontological applications (in the order of microns). While several algorithms have been proposed to minimize these errors in conventional phase shifting interferometry, the estimation of the exact phase step and consequently the interference phase distribution in the presence of error sources remains the main source of difficulty in fringe projection systems. By using Carré's phase estimator, the error in the phase shift among fringe patterns was revealed. Therefore, the need to design a set of eight-frame algorithms for PSP immune to systematic errors, such as higher harmonics in the intensity signal, detuning, nonlinear response of photodetectors, random intensity noise and vibrations [26] in these measures becomes essential as shown in Fig. 3.14.

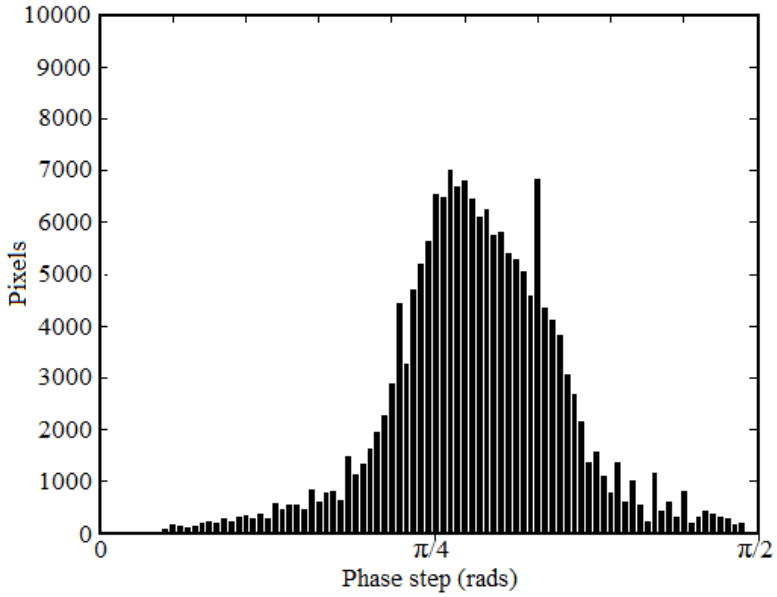

Fig. 3.14: Phase estimator of images achieved from semi-fossilized samples. The ideal phase step is $\pi/4$.

For the development of the best mathematical method for processing the phase shift, several comparisons have been made considering the immunity to errors and miscalibrations of each of the algorithms mentioned above (Fig. 3.15). Accordingly, the width and shape of the histogram represent the variation of phase shifts.

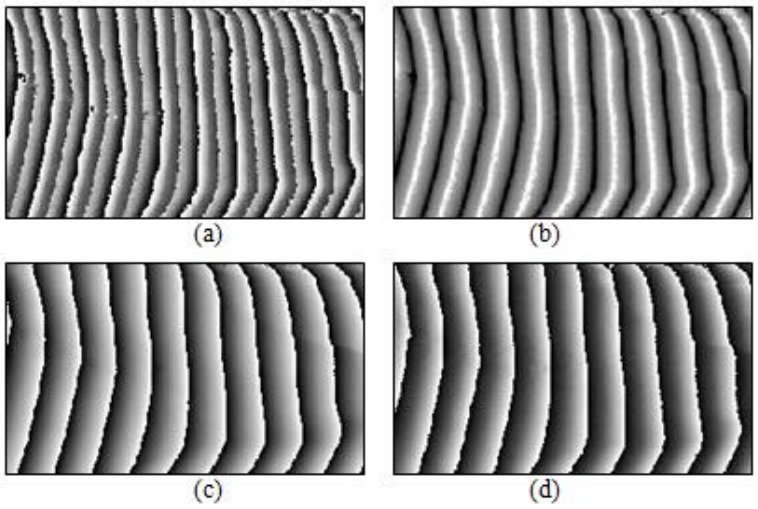

Fig. 3.15: A section of the wrapped phase achieved from experimental images. (a) Schmit's filter. (b) Carré's filter. (c) Hibino's filter. (d) Surrel (N+1) bucket filter.

For these fringe patterns, it is evident that Carré's approach is susceptible to higher-order harmonics in the signal [28]. Filters reported previously in [30] have a good fitting to phase miscalibrations, but in the case of turbulences this method is not recommendable. Results from well-known algorithms, as proposed by Schmit (Fig. 3.15(a)) and Carré (Fig. 3.15(b)), show a high sensitivity to systematic errors. Hibino and Surrel (Figs. 3.15(c) and 3.15(d) respectively) methods are more sophisticated in correcting errors, but there are some inconsistencies in the

form of the wrapped phase. Least-square filter in Fig. 3.16(a) is enough for most applications, because many do not require a maximum level of immunity to detuning and miscalibrations of the phase shifts. Methods proposed have the robustness to manage interferograms with physical limitations and the intrinsically experimental errors present in this kind of measures. The first one is the well-known least-square eight-frame filter, the second corresponds with an algorithm specialized in compensating the phase shift linear detuning error, while the third algorithm is designed to compensate the linear bias variation error and the fourth is an algorithm that simultaneously compensates both kind of errors. However, a successful result depends on two main facts, the algorithm and the kind of errors and noise present in the set of frames measured.

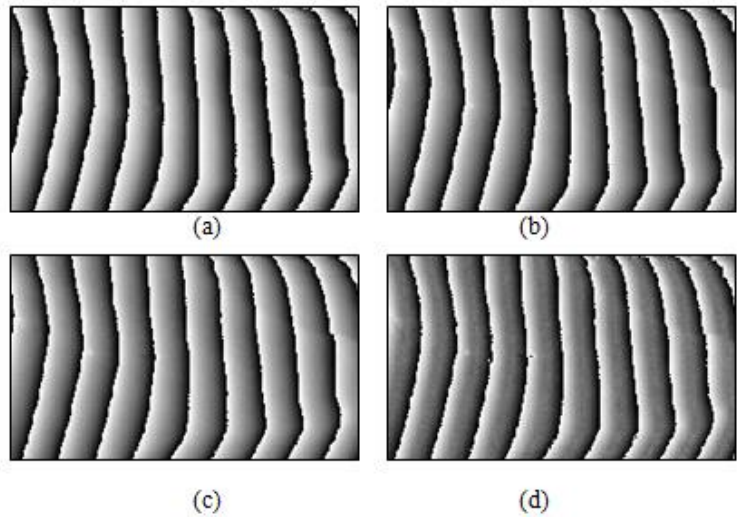

Fig. 3.16: A section of the wrapped phase achieved from experimental images. (a) Least-square filter. (b) MDE filter, cut off frequencies in 0, $\pi/4$, $\pi/4$, $\pi/2$, π, $3\pi/4$, $3\pi/4$. (c) MBE filter, cut-offs in 0, 0, $\pi/4$, $\pi/2$, π, π, $3\pi/4$. (d) DBE filter, cut-offs in 0, 0, $\pi/4$, $\pi/4$, $\pi/2$, π, $3\pi/4$.

In addition, the evaluation of intensities can be made by plotting a linear slice across fringe patterns and analyzing the profile of the phase as in Fig. 3.17. SNR evaluation of our proposed

methods is significantly lower. The MBE algorithm shown in Fig. 3.16(c) has the better immunity to experimental errors in this FPP arrangement and these samples in particular.

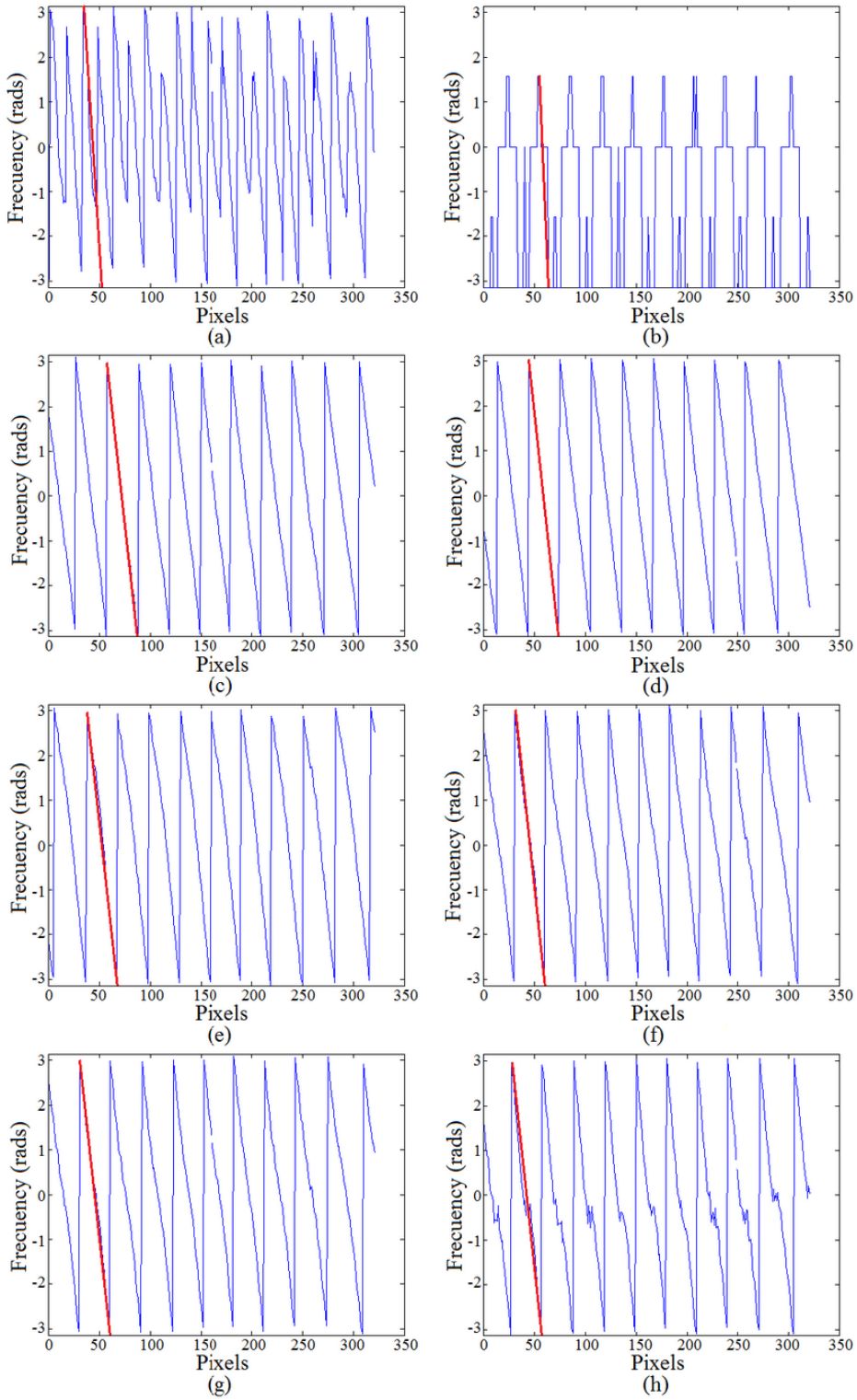

Fig. 3.17: A graphed horizontal line of each image shown in Fig. 3.15 (a-d) and Fig. 3.16 (e-h) respectively.

These results are consistent with the unwrapped heights map, and it gives the right step for the analyses. A textured map of unwrapped phase is shown in Fig. 3.18. When the algorithm is limited in suppressing errors, we generally need more expensive equipment for the experiment to compensate them. On the other hand, having a good algorithm and considering the particular experimental conditions, more economic equipment will be enough to cover the needs of precision and accuracy of the experiment.

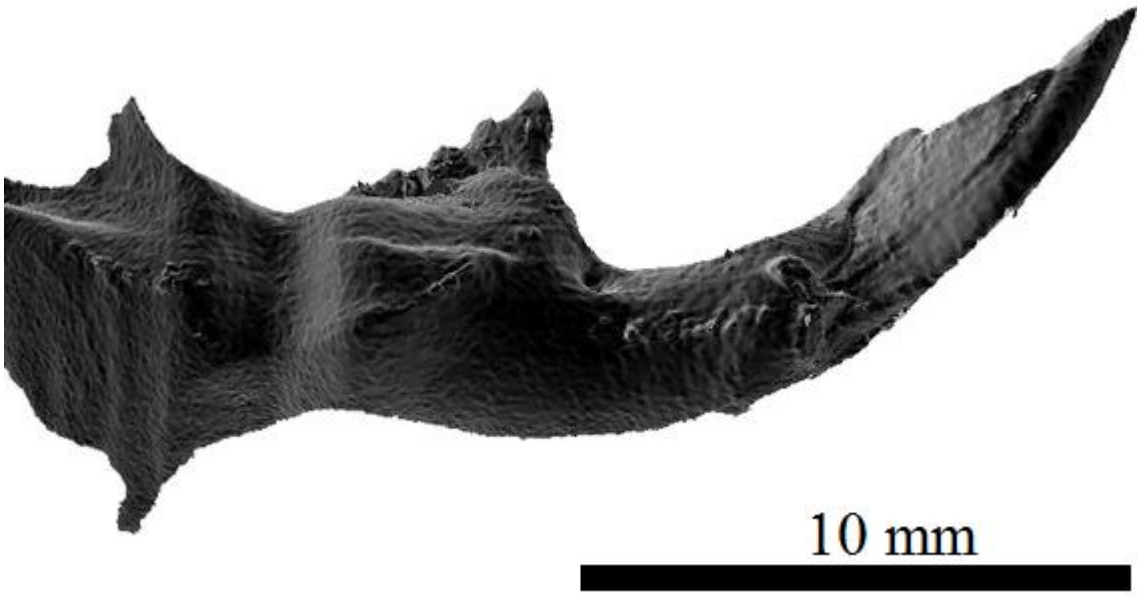

Fig. 3.18: Texture mapping onto the calculated 3D shape distribution.

Most eight step algorithms are centered at $\pi/2$ [31]; however, as the error distribution is greater for each step, a filter centered in a further step ($\pi/4$ in this case) and immune to detuning (given the dispersion of the phase steps in Fig. 3.14) is needed to compensate experimental errors. In the experiment conducted, objects under study were small (~20mm), and the technique proved to

be a simple, cheap, and flexible method to be applied in areas that use phase shifting interferometry, but also other fields like paleontology, anthropology, and the sort. For instance, studies that need high resolution images for a posteriori scientific analyses, as well as morphological studies that involve ancient DNA preservation and reconstruction of semi-fossilized samples at different scales, are some of the applications and advantages of the described technique.

References

1. J. H. Bruning, D. R. Herriott, J. E. Gallagher, D. P. Rosenfeld, A. D. White, and D. J. Brangaccio, "Digital wavefront measuring interferometry for testing optical surfaces and lenses," Appl. Opt. **13**(11), 2693–2703 (1974).

2. J. Schwider, R. Burow, K. E. Elssner, J. Grzanna, R. Spolaczyk, and K. Merkel, "Digital wave-front measuring interferometry: some systematic error sources," Appl. Opt. **22**(21), 3421–3432 (1983).

3. P. Groot, "Derivation of algorithms for phase-shifting interferometry using the concept of a data-sampling window," Appl. Opt. **34**(22), 4723–4730 (1995).

4. K. Freischlad, and C. L. Koliopoulos, "Fourier description of digital phase measuring interferometry," J. Opt. Soc. Am. A **7**(4), 542–551 (1990).

5. Y. Surrel, "Design of algorithms for phase measurements by the use of phase stepping," Appl. Opt. **35**(1), 51–60 (1996).

6. D. W. Phillion, "General methods for generating phase-shifting interferometry algorithms," Appl. Opt. **36**, 8098-8115 (1997).

7. J. Schmit, and K. Creath, "Extended averaging technique for derivation of error-compensating algorithms in phase-shifting interferometry," Appl. Opt. **34**(19), 3610–3619 (1995).

8. J. F. Mosiño, J. C. Gutiérrez-García, T. A. Gutiérrez-García, and J. M. Macías-Preza, "Two-frame algorithm to design quadrature filters in phase shifting interferometry," Opt. Express **18**(24), 24405–24411 (2010).

9. D. Malacara, Optical shop testing, 3rd. Edition, (J. Wiley and Sons Inc., Hoboken, New Jersey, 2007).

10. M. Chang, D. Wan, On-line automated phase-measuring profilometry, Opt. Laser Eng. **15**(2), 127–139 (1991).

11. X. F. Meng, X. Peng, L. Z. Cai, A. M. Li, J. P. Guo, Y. R. Wang, Wavefront reconstruction and three-dimensional shape measurement by two-step dc-term-suppressed phase-shifted intensities, Opt. Lett. **34**(8), 1210–1212 (2009).

12. A. Martínez, J. A. Rayas, R. R. Cordero, D. Baliero, F. Labbe, "Leaf cuticle topography retrieved by using fringe projection," Opt. Lasers Eng. **50**(4), 231-235 (2012).

13. X. Su, G. von Bally, D. Vukicevic, Phase-stepping grating profilometry: utilization of intensity modulation analysis in complex objects evaluation, Opt. Commun. **98**, 141–150 (1993).

14. Y. Surrel, "Design of phase-detection algorithms insensitive to bias modulation," Appl. Opt. **36**(4), 805–807 (1997).

15. H. Schreiber, J. H. Brunning, and J. E. Greivenkamp, "Phase shifting interferometry," in Optical Shop Testing, D. Malacara ed., (John Wiley & Sons, Inc., Hoboken, New Jersey 2007).

16. M. Afifi, K. Nassim, and S. Rachafi, "Five-frame phase-shifting algorithm insensitive to diode laser power variation," Opt. Commun. **197**(1-3), 37–42 (2001).

17. J. F. Mosiño, M. Servin, J. C. Estrada, and J. A. Quiroga, "Phasorial analysis of detuning error in temporal phase shifting algorithms," Opt. Express **17**(7), 5618–5623 (2009).

18. J. F. Mosiño, D. M. Doblado, and D. M. Hernández, "Calculus of exact detuning phase shift error in temporal phase shifting algorithms," Opt. Express **17**(18), 15766–15771 (2009).

19. J. F. Mosiño, D. Malacara Doblado, and D. Malacara Hernández, "A method to design tunable quadrature filters in phase shifting interferometry," Opt. Express **17**, 15772-15777 (2009).

20. J. F. Mosiño, J. C. Gutiérrez-García, T. A. Gutiérrez-García, F. Castillo, M. A. García-González, and V. A. Gutiérrez-García, "Algorithm for phase extraction from a set of interferograms with arbitrary phase shifts," Opt. Express **19**, 4908-4923 (2011).

21. J. C. Gutiérrez-García, J. F. Mosiño, Amalia Martínez, T. A. Gutiérrez-García, E. Vázquez-Domínguez, and J. Arroyo-Cabrales, "Practical eight-frame algorithms for fringe projection profilometry," Opt. Express **21**, 903-917 (2013).

22. P. Almeida Magalhaes, P. Smith Neto, and C. Sperb Barcellos, "Phase shifting technique using generalization of Carre algorithm with many images," Optical Review **16**(4), 432-441 (2009).

23. C. Rathjen, "Statistical properties of phase-shift algorithms," J. Opt. Soc. Am. A **12**, 1997-2008 (1995).

24. C. S. Guo, L. Zhang, H. T. Wang, J. Liao, and Y. Y. Zhu, “Phase-shifting error and its elimination in phase-shifting digital holography,” Opt. Lett. **27**, 1687-1689 (2002).

25. K. Hibino, B. F. Oreb, D. I. Farrant, and K. G. Larkin, “Phase-shifting algorithms for nonlinear and spatially nonuniform phase shifts,” J. Opt. Soc. Am. A **14**(4), 918–930 (1997).

26. P. D. Ruiz, J. M. Huntley, and G. H. Kaufmann, “Adaptive phase-shifting algorithm for temporal phase evaluation,” J. Opt. Soc. Am. A **20**, 325-332 (2003).

27. Y. Surrel, “Phase stepping: a new self-calibrating algorithm,” Appl. Opt. **32**(19), 3598–3600 (1993).

28. K. Creath, “Temporal phase measurement methods,” in *Interferogram Analysis*, D. W. Robinson and G. T. Reid, eds. (Institute of Physics, 1993).

29. J. M. Huntley, “Automated Analysis of Speckle Interferograms,” in *Digital Speckle Pattern Interferometry and Related Techniques*, P. K. Rastogi, ed. (Wiley, 2001).

30. K. Creath and J. Schmit, “N-point spatial phase measurement techniques for nondestructive testing,” Opt. Lasers Eng. **24**(5-6), 365–379 (1996).

31. J. A. N. Buytaert, and J. J. J. Dirckx, “Study of the performance of 84 phase-shifting algorithms for interferometry,” J. Opt. **40**(3), 114-131 (2011).

Chapter 4

Experimental part

4.1 Preliminary studies

The optical 3D profilometry has revealed several qualities that make it particularly suitable for the study of fossil and semi fossil bone, such as they cause no alteration to the studied surface. To obtain the information of the topography from bone samples, a series of eight frame experimental patterns were obtained from a fringe projection profilometry system [1, 2] and processed with the PSA proposed to obtain the topography. A preliminary test performed is shown in Fig. 4.1.

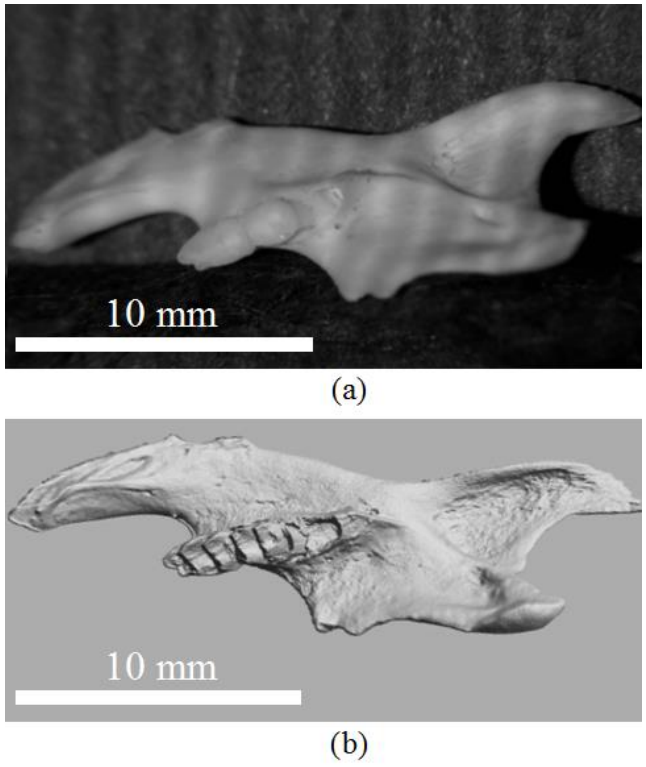

Fig. 4.1: Initial tests with specimens of maxillary contemporary mammals: (a) modern bone and (b) its recovered topography.

The objects can be studied under atmospheric conditions and complex surface features such as broadside inclinations, symmetry and number of microstriations, are accessible for quantitative evaluation [3]. Prior to the preparation of the semi-fossilized samples, several tests were

performed on samples from the maxillary of contemporary specimens to verify both, the feasibility of the technique on semi fossilized samples, and sample handling, so that they were not contaminated with modern DNA or fractured during placement in the optical arrangement (Fig. 4.2).

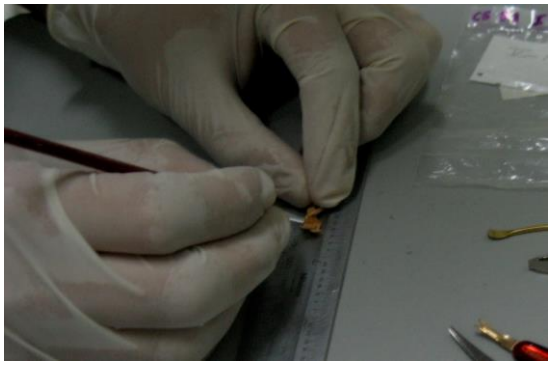

(a)

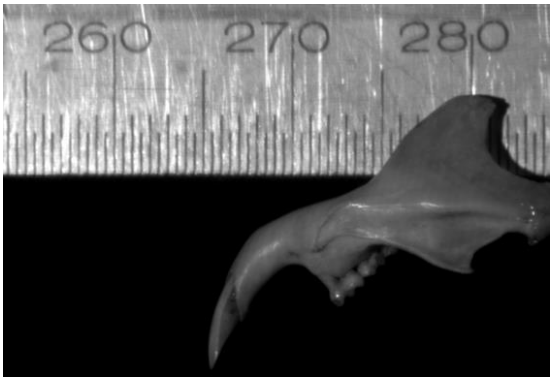

(b)

Fig. 4.2: (a) Preparation and sample handling. (b) Reference plane of the sample.

Based on preliminary studies showing the number of variables to be considered to recover the 3D cloud of points of the samples, it was concluded that an appropriate algorithm to retrieve the wrapped phase would be sufficient to compensate for many of the errors in the measurements due to the quality of the laboratory materials used for the optical system. Errors considered for this purpose, to mention a few, were systematic errors, such as the nonlinearity of the CCD sensors, vibration, reflections from the optical elements, relative phase between pixels, etc.

4.2 Experimental arrangement for fringe projection profilometry

The recovery of the surface characteristics of the sample was performed using the fringe projection profilometry method. The optical system used was composed of a laptop with a frame grabber attached to a multimedia LCD projector, with a converging lens with a focal length of 10 cm on a sliding base; on its right side we fitted a PixeLINK PL-A741 CCD camera with a resolution of 1280x1024 pixels in grayscale ranging from 0 to 255, with a f5/6 zoom lens and a rotary mounting. The spatial resolution of the captured images was 53 pixels per millimeter (mm). The optical axis of the camera was perpendicular to the reference plane, while the line connecting the projector and camera were parallel to the reference plane accordingly to [4]. The distance between the CCD and the projector d was 80 mm, the distance between CCD and the reference plane was 225 mm, and between the projector and the reference plane was 239 mm. The full schematic arrangement used to capture the frames is shown in Fig. 4.3.

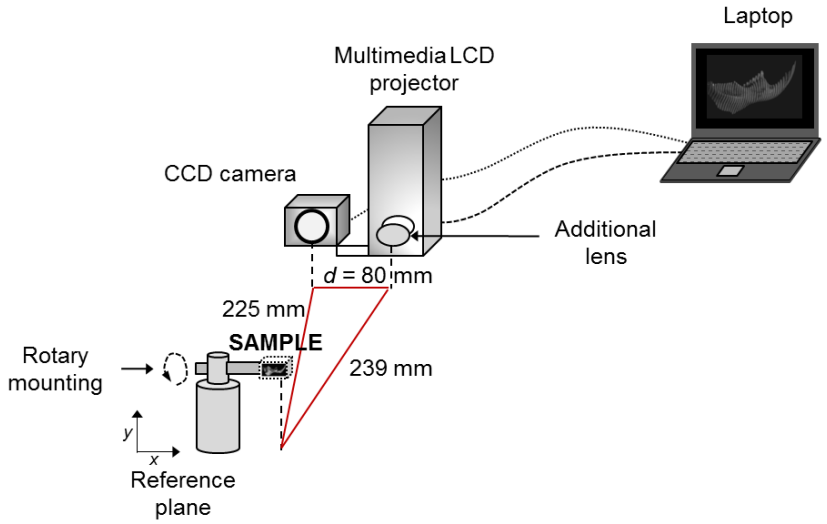

Fig. 4.3: Optical set up specifications for the FPP system used in this study for the recovery of a 3-D image of a hemimandible sample.

The entire system was set up in accordance with the sample dimensions (approximately 20 mm in length, 15 mm in height and 3 mm in depth). All the calibrations of the optical set up were made following standard procedures [5] and parameters, like gamma [6], intensity [7] and sinusoidal error [8]. The sample was fixed to the rotary platform by applying a delicate brushstroke with a paleontological consolidant (an adhesive routinely employed to repair or consolidate small fragments from crushed, broken or fragile samples), specifically used during the excavation of our fossil material [9]; this substance worked as an interphase that joined the mounting with the farthest segment of the mandible. The consolidant was strong enough to firmly hold the hemimandible (weight=0.16 grams), and once dry, it was easily removed from the mounting and the sample. The sample was mounted on a rotating stage in order to enable 360º scanning of the object for a reconstruction of a full 3D image (Fig. 4.4).

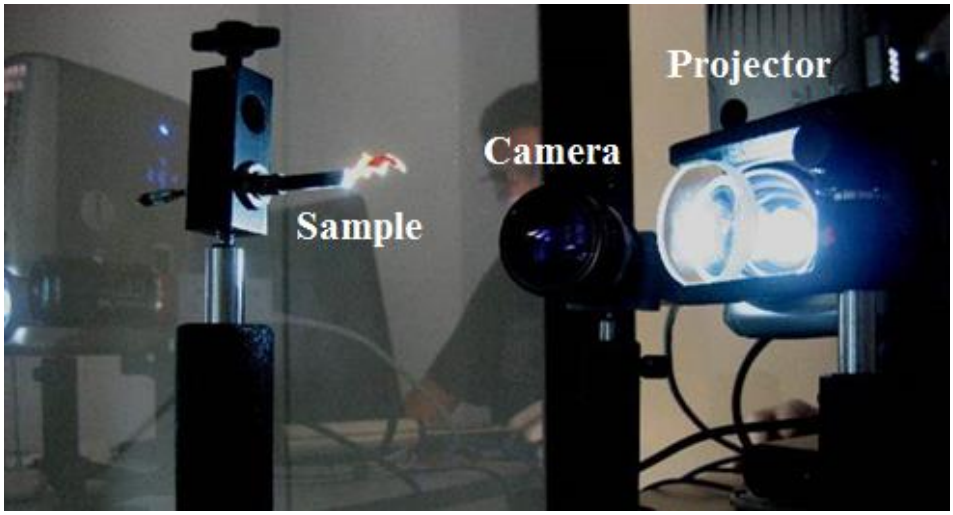

Fig. 4.4: Fringe projection system.

Then, eight images were recorded by the CCD and a low pass filter is applied to eliminate random noise phase. These images with the projected fringes over the object were captured every 60º of rotation of the sample to reconstruct a 3D model of the fossil (topography was

evaluated to each one of these periods). Computational PSA algorithms are implemented based on image processing to decode this information from wrapped phase map and get the physical dimensions of the digitalized sample.

4.3 Sample preparation

We used a semi-fossilized hemimandible from a rodent identified at that time to belong to the genus *Ototylomys* [10] (INAH number B6M13-19), which was used for DNA extraction after image acquisition [11]. The FPP method was applied to acquire morphological data from these specimens that were collected from the "El Toro" chamber in the Loltún caves (located in the state of Yucatán, México) over a period of several decades. To ensure optimum performance of the system, the surfaces studied should have the following properties according [3]: color must be bright to ensure that most of the incident light is reflected back to the CCD; color must be homogeneous (significant albedo disparity may cause focusing errors); only a little translucency may be accepted in order to allow the system to focus on the physical surface and the roughness may not exceed the focusing boundaries. Fossils and sub-fossils bones have been proven to usually meet these requirements excellently. An exception, however, is the material with inhomogeneous mineralization or demineralization, showing a range of colors and varying translucency; in this case, the intensity of the reflected light overrides the sensitivity of the detector system, causing saturation and defocusing in the images of the acquired surface [3]. Consolidant effect on the optical characteristics of the samples is shown in Fig. 4.5.

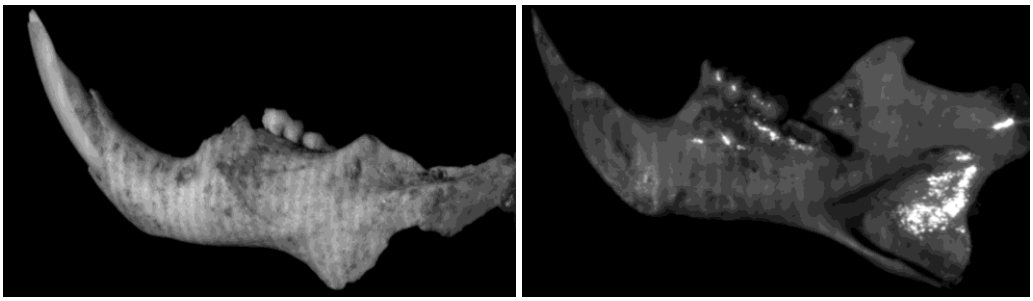

(a) (b)

Fig. 4.5: Effect of the consolidant in the samples provided from INAH. (a) Sample with a lack of consolidant. (b) Sample with too much consolidant.

The main difficult in the sample handling of this kind of materials is that they must be free of genetic contaminants since they will be analyzed later using the PCR method of analysis (which implies the destruction of the sample). The retrieval of ancient DNA sequences is uncertain mainly by the fact that very little and often the DNA does not survive in ancient bones, whereas contemporary DNA is pervasive in the environment. For the handling of the sample, we used protective clothing and face shields and took routine precautions to avoid human contamination of ancient samples [12]. Also, all instruments, equipment and the working area were sterilized with bleach, alcohol and/or ultraviolet (UV) radiation [13] (ensuring that all instruments were sterilized based on the sterilization time for disinfection at 254 nm), eliminating any biological contaminant present in the optical arrangement Additionally, no other ancient or modern biological materials were ever used before in the working room.

The semi fossilized material was taken out of its sealing container and with caution removed the excess of consolidate material to faithfully obtain morphologic and optic characteristics of the piece. Finally, the sample was fixed on a rotatory mounting plate by using inert resin.

4.4 Optical system and procedure

The non-linear nature of the FPP system introduces additional phase errors that can be compensated by using a large number of phase shift fringe patterns. However, this increases computational time and space, reducing the speed of the shape and accuracy of measurement. In addition, it depends directly on the available algorithms for calculating the wrapped phase [7, 14]. We used an effective phase shifting algorithm, the MBE phase filter, which was recently developed specifically to prevent and even compensate for these systematic errors by using only eight frames to obtain the wrapped phase [15].

As mentioned, modern or ancient DNA should not be exposed to high radiative coherent light sources because of their ionizing effect that is a damaging agent for DNA [16-19]. In order to minimize the exposure of the sample to white light (incoherent light), each of the eight frames needed for the MBE filter had an acquisition time of 20 milliseconds (ms), giving a short exposure time (<1 second) for the complete optical system. Accordingly, we took eight frames (spaced spectrally $\pi/4$) with periods of 8 and 128 pixels per fringe (0.125 mm and 2 mm respectively), as shown in Fig. 4.6.

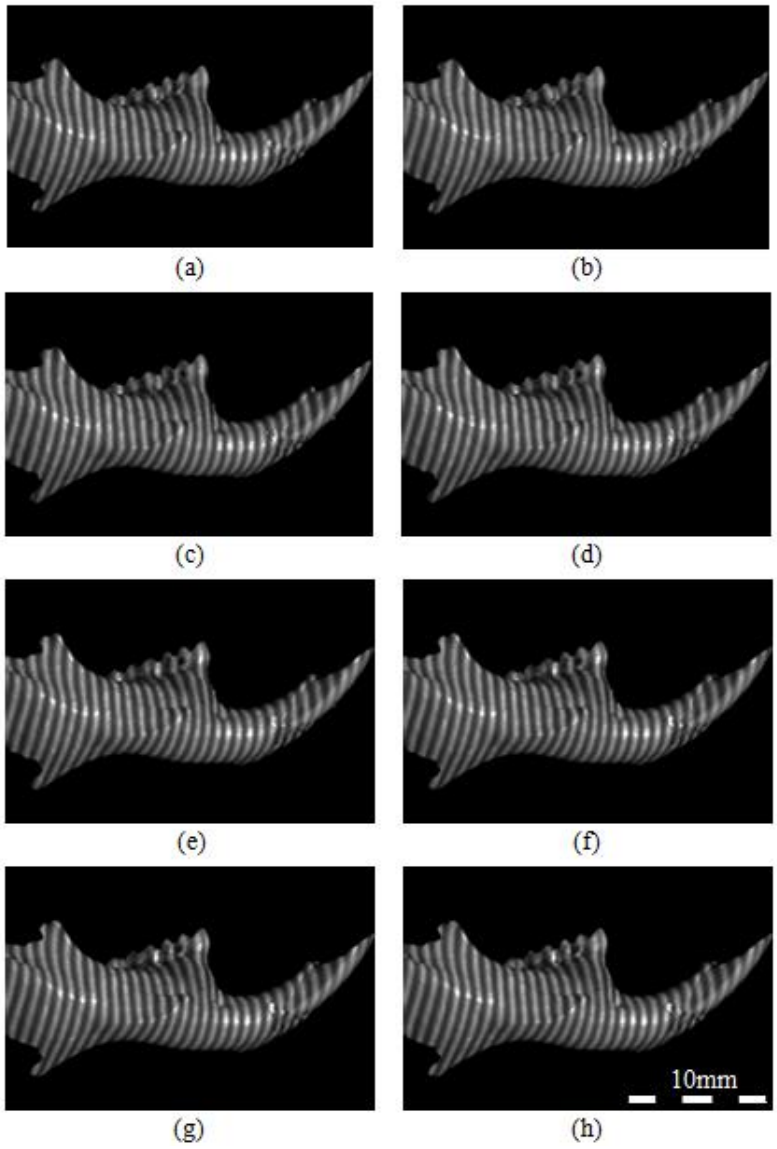

Fig. 4.6: Intensity patterns acquired from a FPP system with periods of 8 pixels per fringe. Phase shift values of the projected fringes are (a) 0, (b) π/4, (c) π/2, (d) 3π/4, (e) π, (f) 5π/4, (g) 3π/2 and (h) 7π/4.

Subsequently, we rotated the sample 60º on its own x axis and acquired eight frames, repeating this until a full 360º rotation had been completed. The use of both 8 and 128 pixels per fringe guarantees a successful detailed recovery of the sample's topography, overcoming the shadows resulting from the sample's irregular surface [20].

4.5 Data analysis

The image processing were implemented in MATLAB v7.12 and LabVIEW v8.2.1. After the gathering process and FPP technique to recover the wrapped phase image, we unwrapped the phase obtained with MBE by using Goldstein's branch cut algorithm, an extraordinarily fast method that requires little memory, successfully unwrapping the phase by minimizing its discontinuities [21, 22]. Once unwrapped, we estimated and subtracted the temporal carrier [23] to obtain the sample's reconstructed topography. Finally, we performed an image render and texturing of the 3D image of the sample using MeshLab 1.3.3 [24]. The image acquisition set up and the processing of data is shown in Fig. 4.7.

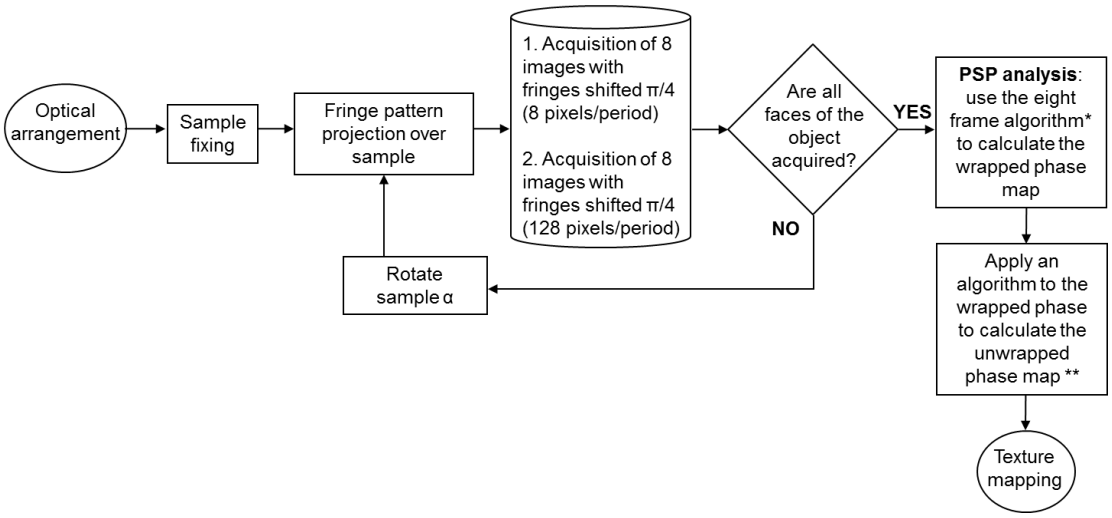

Fig. 4.7: Flowchart of the procedure employed in this study, where: α = angle (60º in this case), * = MBE algorithm (Gutiérrez-García et al., 2013), and ** = Goldstein algorithm. OTY: name given to the white light system together with the phase shifting algorithm filter, based on the fact that it was developed for use on *Ototylomys* samples.

We named the white light system together with the phase shifting algorithm filter as "OTY", which are letters of *Ototylomys*, given that it was developed for use on samples of this genus.

4.6 Results

A total of 44 hemimandibles of 2 species of mammals were analyzed, and 96 frames from each hemimandible were obtained, divided in two sets of 48 frames that had 8 and 128 pixels/period, respectively (magnitude maps obtained are shown in Fig. 4.8).

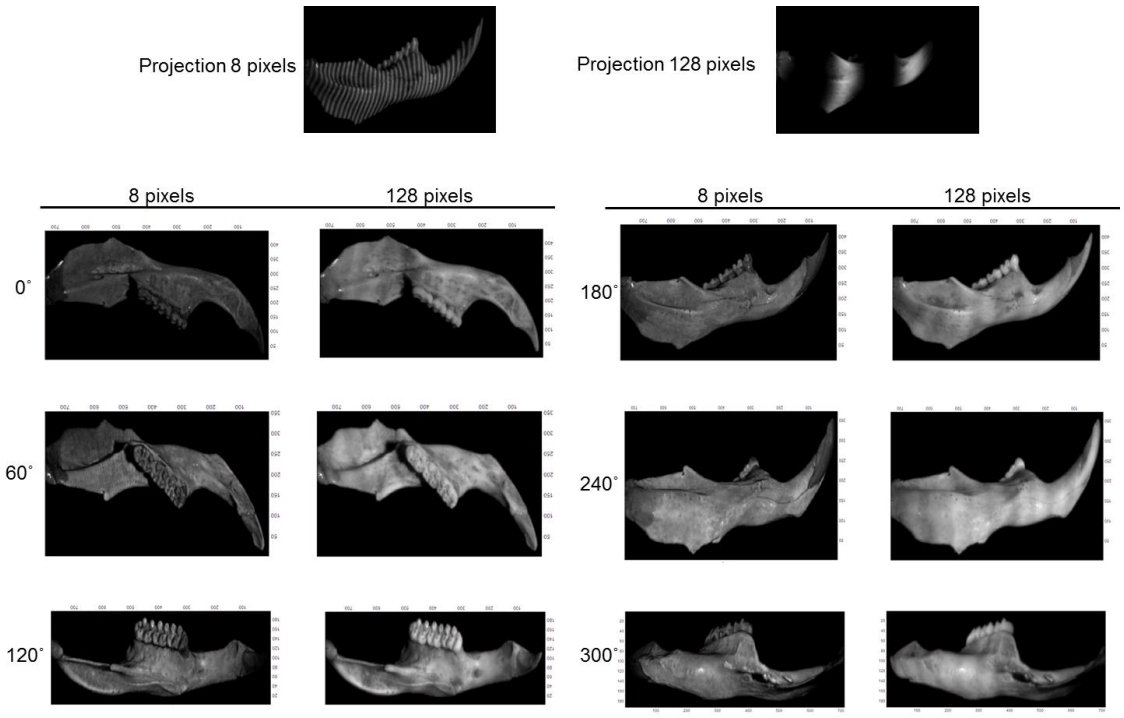

Fig. 4.8: Magnitude maps of the sample obtained every 60º for 8 and 128 pixels/period. The images show the resolution and detail levels given the number of fringes projected over the sample. The measurements' accuracy of surface and depth depends on the number of projected fringes, which include as many as the system can display (8 pixels/period for each fringe in this case). When the acquisition of details is difficult, a wider fringe is required (based on our sample size, we used 128 pixels).

In most optical methods, it is suggested to use a treatment of the sample (e.g., covering it with color) to ensure optimum performance and avoid reflections or other undesirable effects [3], like

scattering, diffraction or dispersion, among others. However, a relevant advantage of our technique is that no such special sample preparation was required to obtain the frame or the processed images, a vital aspect to ensure the integrity of the sample (e.g., less risk of contamination by chemical agents or modern materials). The sequence followed to acquire the topographic maps included the fringes projection [Fig. 4.9(a)], the wrapped phase [Fig. 4.9(b)], the unwrapped phase [Fig. 4.9(c)], and the carrier compensation procedure [Fig. 4.9(d)]. Image processing was performed without any spatial filtering to preserve the most detail in the final 3D images [Fig, 4.9(e)].

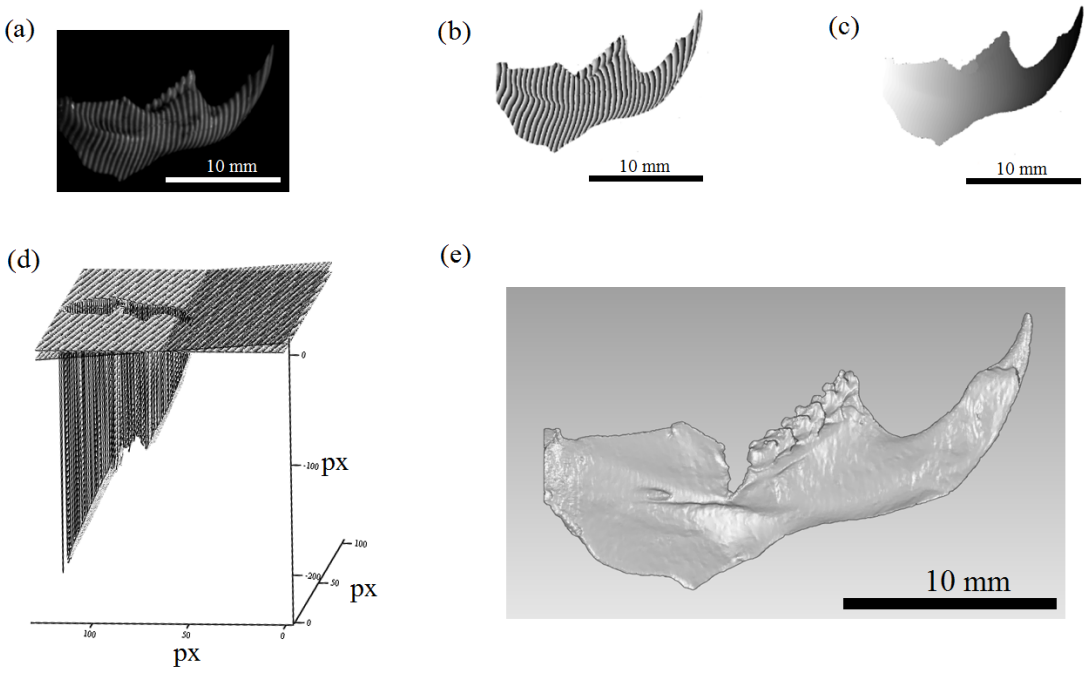

Fig. 4.9: Process applied to recover the topography of the fossil sample. Where: (a) image captured by the CCD of the fringe projection on the sample, (b) wrapped phase obtained of the 8 frames after applying the MBE filter, (c) unwrapped phase map, (d) phase carrier compensation, and (e) surface of one of the views of the fossil recovered.

The average resolution of the acquired images was 18.8 µm/pixel. It should be noted that this technique does not require the use of fiduciary markers for aligning different rotations of the object to attain the 3D object, and we captured views every 60º in order to scan the entire piece. Each of the six views processed with the optical system are shown in Fig. 4.10, where it can be appreciated that some regions of the sample have no information.

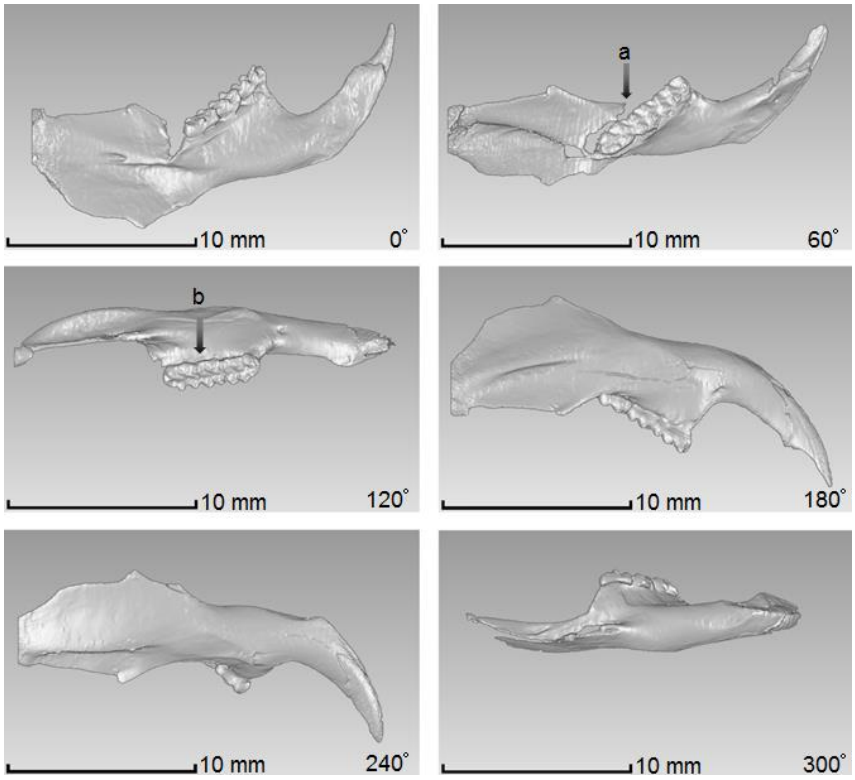

Fig. 4.10: Processed views of a fossil sample acquired by the optical FPP system OTY. Each view is re-oriented 60º degrees with respect to the prior. Where: "a" indicates a zone that has no information at 60º in this stage of the process and will be corrected with the information of the next view, as is shown in "b".

These regions are caused by the shadow created on the sample when projecting the fringes, reflecting the areas where no information can be obtained from the surface. However, the redundancy of the information is completed from all the set of images, which guarantees that

each region is captured by the camera more than once; therefore, by combining each of the six views in a complete 3D image, these regions are integrated and the missing gaps are filled (Fig. 4.11).

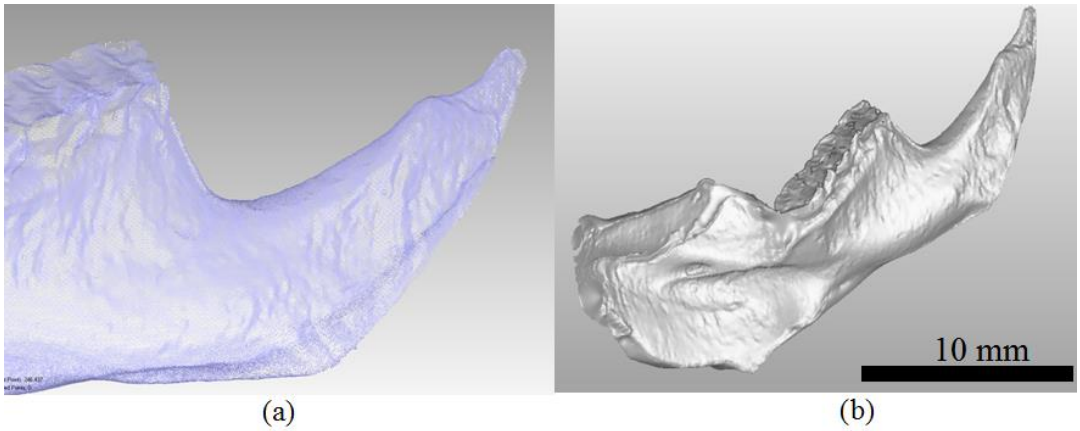

Fig. 4.11: Full 3-D image of the reconstructed fossil after merging all the six views. (a) Cloud of points, (b) Final mesh.

In addition, by using the topographic maps gathered from each of the six faces (at every 60º angle) of the tested sample, we were able to construct the 3D image including high fidelity dimensions and recovering all of its morphological details. Furthermore, digitized samples provide an exact 2D measurement regarding the handmade measurements currently carried out in palaeontologia (Fig. 4.12).

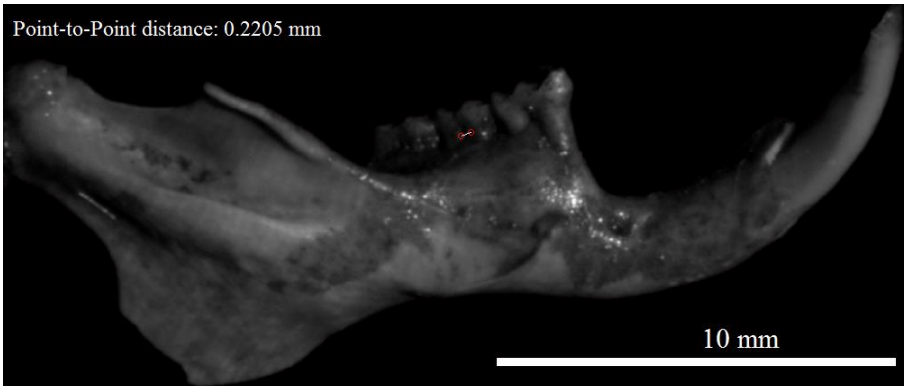

Fig. 4.12: Distances between points (2D).

4.7 Discussion

Several methods have been used to non-destructively image fossils in 3D [25-28]; however, most are based on ionizing radiation (e.g., X-rays, micro CT), which can result in molecular damage. A good comparison of these techniques was made in [29-31], and discusses a wide variety of 3D imaging techniques applicable to fossils and their suitability for different materials. When the crucial aim is to recover DNA from fossils, it is vital to use techniques that will cause as less molecular damage as possible, and those based on white light are a practical choice. Indeed, a segment of the white light spectrum has been used to describe the fossil's molecular content [32].

Despite its advantages, the FPP system using white light has rarely been used to obtain 3D-images of biological samples. This method has only been explored via simulations under ideal laboratory conditions, mainly because of the complexities involved when working with it, including the need to consider specific features of the surface being analyzed, the optical set up requirements -like in the present case where, due to the fragility of the fossil, an optical rotation mount had to be designed to hold the piece-, potential bias errors, image acquisition defects and additional errors during image processing [3, 21 (and references therein)].

In this study, we ensured the optimum performance of the system by adapting the optical set up to the sample size and by using the algorithm MBE [15], which reduces common errors during the processing of the frames, such as miscalibrations, bias and detuning errors. Because MBE is a real high bandwidth phase filter, it has the advantage that it minimizes the image's distortion and does not perform, like other common algorithms (e.g., Carré or N + 1 Bucket; by [33] and [34], respectively), as a low-pass filter. This final outcome yields the most accurate reconstruction of the object and with greater and enhanced detail than any other PSA that could be used for samples like our fossils. The advantage of optical techniques in the study of fossil

and semi fossil bone is that non-contact technique, allowing the investigation of fragile and poorly preserved surfaces. The high resolution and fast measuring rate of this method make it an alternative to scanning electron microscopy (SEM) or optoelectronic scanning methods if topography is to be visualized.

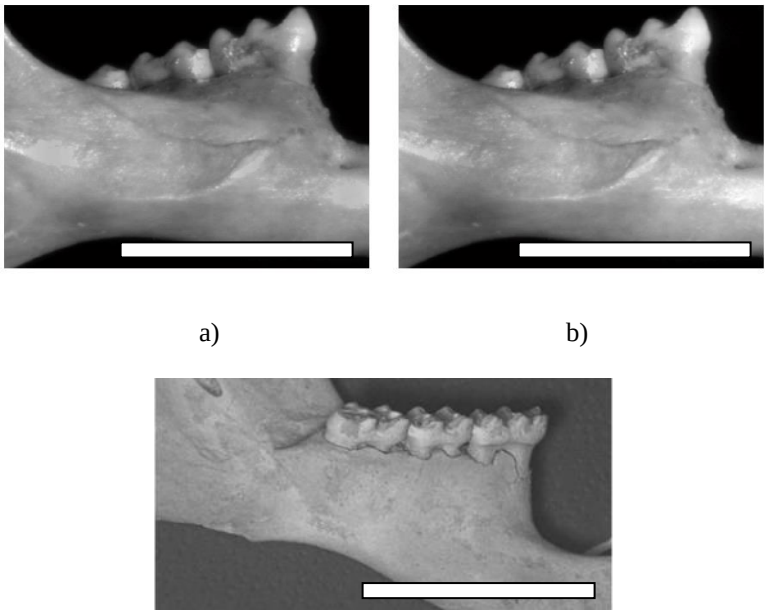

a) b)

c)

Fig. 4.13: Differences between (a) N+1-bucket filter, (b) proposed MBE eight step filter and (c) scanning electron microscope (SEM). Scale bar is 5 mm.

Due characteristics of the semi-fossilized materials, comparing MBE filter side by side N-bucket filter to recover the wrapped phase, enable us to assess the optimal filter for semi fossilized materials, compensating light variations and errors inherent to the optical system. Therefore, it is necessary to improve the surface reflectivity of the fossils and the contrast of fringe pattern to reduce the errors. The cloud of points plotted represents the magnitude of the recovered real points, and it is possible to realize the 3D reconstruction of the fossil and carry out comparative

phylogeography analyzes and in the like. A filter analysis of several filters applied to reconstruct the 3D shape is shown in Fig. 4.14.

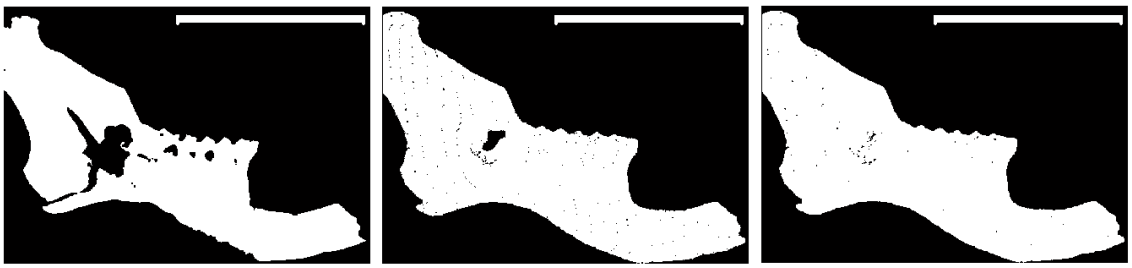

Fig. 4.14: (a) N+1 bucket algorithm, 31.7461 % of useful points to reconstruct the cloud of points (139,367 pixels). (b) MDE filter, 37.0228% of useful points (162,532 pixels). (c) MBE filter, 37.0663% of useful points (162,723 pixels). Scale bar is 10 mm.

This is the main advantage of designing a filter to fit the experiment as the MBE filter. A comparison between (a) and (c) is shown in Fig. 4.15.

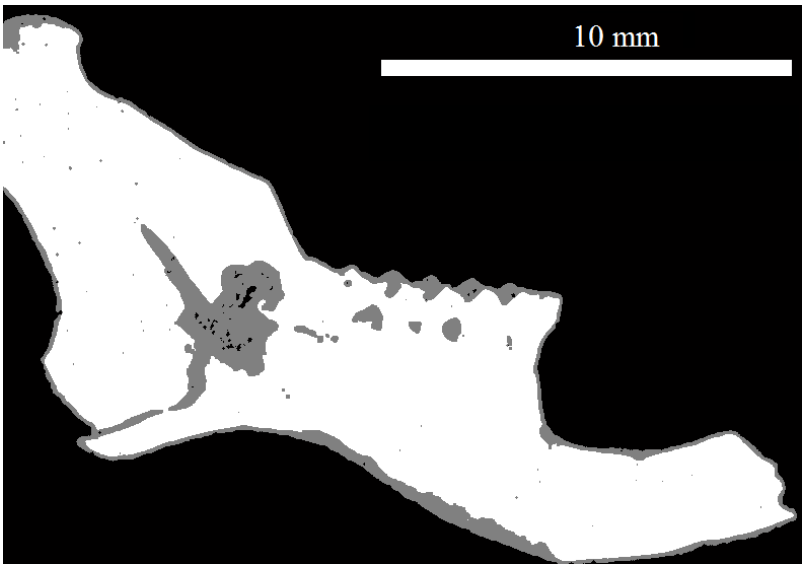

Fig. 4.15: Comparison of the phase map recovered from a single fossil sample. (a) N+1 bucket filter phase map is depicted in white. (b) Phase map recovered with MBE filter is depicted in white + gray.

Processing the phase map and texturing the recovered cloud of points, it is clearly the effectiveness of the designed filter. In Fig. 4.16, information retrieval for the cloud of points is higher in the filter processing using the proposed MBE filter than others.

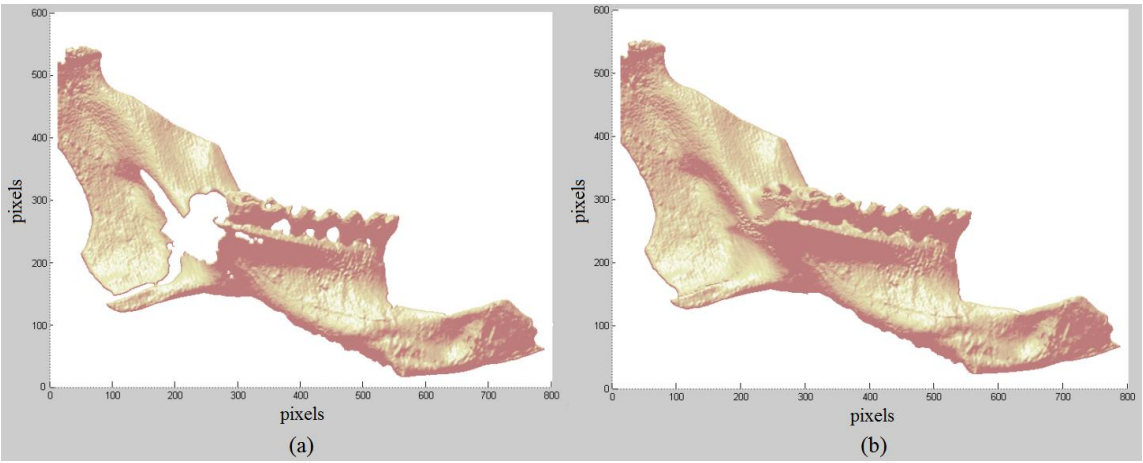

Fig. 4.16: The N+1-bucket algorithm (a) compared against the MBE filter (b).

Moreover, the high 3D-image resolution we obtained (18.8 μm) is comparable with those achieved with white light and well known algorithms [35]. Furthermore, using this technique, the resolution is comparable with more expensive 3-D imaging techniques also used for fossils, as laser scanning (>50 μm), magnetic resonance imaging (>10 μm), neutron tomography (>30 μm). Also, using a distinct lens it can achieve micro-CT resolution (>1 μm) [30, 31], considering that the current resolution limit for a white light image system is around 0.5 μm because diffraction effects limit the maximum possible resolution [36]. The camera exposure time is crucial to guarantee a high intensity modulation of the captured fringe patterns along dark regions of the image, regardless of image saturation occurring on bright regions [37]. In our case, an exposure of 20 ms per frame was sufficient to avoid poor measurement accuracy and was also a short enough exposure to avoid harming the fossil, given that prolonged exposure to visible light can damage DNA [16, 18, 38, 39]. The different techniques and sequential steps we followed proved useful to obtain detailed measurements such as area, volume and distance

between different points of the hemimandible, avoiding the need to manually handle the sample and the risk of damaging or contaminating it. Furthermore, the digital 3D topography can be used in morphometric studies [40], minimizing the errors associated with manual measurement tools. Moreover, it is useful for 2D and 3D studies such as images properties and color manipulation, geometric operations, segmentation analysis and linear and nonlinear filters for spatial and frequency-domain processing [41], as shown in Fig. 4.17.

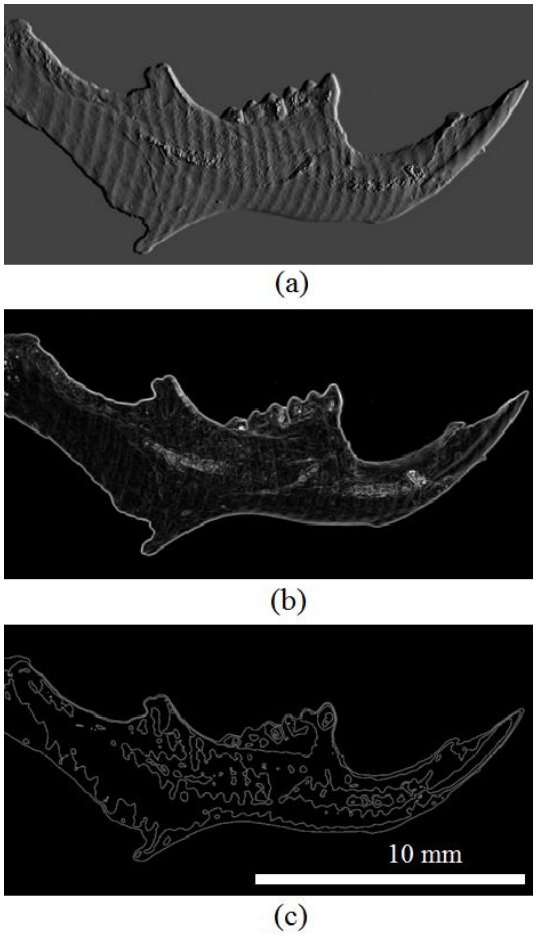

Fig. 4.17: Examples of analyses that can be performed with the obtained data from the fossils: (a) denoting the relief (emboss filter), (b) detecting edges and transitions (sobel filter), (c) study of the roughness and waviness of a sample (topography filter).

Additional applications of our technique include basic morphological operations in 3D images (distance transform, dilation, erosion, opening), 3D restoration, cropping, padding,

resizing, out-of-core image processing and active contour segmentation, just to mention a few. With this technique, scaled 3D models and high-resolution images can be obtained for any fossil or sample, allowing their preservation in extreme detail, crucial in cases where they have to be destroyed. Due to the fact that this is a surface technique, there was no need to apply a high radiative energy source like laser scanning, or to produce a penetration depth like CT techniques. Furthermore, although the mean goal is to recover a higher resolution of a 3D shape onto a cloud of data and to expose the sample the least possible to radiative energy, this method is rather simple and fast, can be performed in a small room and at a low cost since it does not require expensive equipment. The main advantages of this FPP technique in comparison with photogrammetry (PG) include: 1) it directly obtains the real topography's height distribution, while PG only acquires an estimation of it, 2) it obtains a complete cloud of points by using 48 frames, while PG needs 200 or more and only gets a dense cloud of points [42]; the latter is because accuracy depends on the number of pictures taken, and 3) it obtains a 3D exact image without any fiducially points, while for PG the alignment of the required fiducial points directly impacts the exactitude of measuring and model scaling.

4.8 Overall

Several methods have been used to acquire images of fossils [25, 28]; however, most of them are based on coherent radiation light, which is also used to perform molecular damage. Nevertheless, when the aim is to recover DNA from fossils, it is necessary the use of harmless techniques. Due to this, those techniques based on white light are a practical choice (e.g. a segment of the white light spectrum has been used to describe fossils molecular content, [32]).

Despite its advantages, the FPP system that uses white light has been briefly used to acquire 3D images of biological samples. This method has not been utilized out of simulations and laboratory conditions due the complexity involved in working with it, which includes take into consideration features of the studied surface, optical set up requirements (e.g. due to the fragility of the fossils, an optical rotation mount was designed to hold the pieces), bias errors, image acquisition defects and additional errors during image processing [3, 21]. In this study, we ensure the optimum performance of the system by adapting the optical set up to the sample size and by using the algorithm MBE [15], which reduces the common errors during the processing of the frames. MBE has the advantage of being a real high bandwidth phase filter that minimizes the distortion of the images, and not acting as a low-pass filter, like some others that are commonly used (e.g. Carré [45] or N + 1 Bucket [34], resulting in a faithful reconstruction of the pieces with greater detail than any other PSA used for this kind of samples.

The high resolution 3D image that we obtained using white light can be compared to those obtained by using laser (e.g. 19 μm, [35]). The camera exposure time is essential to ensure high intensity modulation of the captured fringe patterns in the dark image regions, regardless of image saturation occurring in the bright image regions [34]. Experimentally, an exposure time of 1/50s per frame acquired was sufficient to obtain an excellent accuracy and to prevent possible damages to the fossils.

The implementation of all of these techniques with their respective considerations is useful to obtain measurements of the fossils, such as area, volume, and distances between different points of the mandible. The availability these digital 3D topographies will also minimize the common errors during measurements for morphometric studies [40, 43, 44]. This technique will allow the printing of scaled 3D models of almost any fossil sample and to obtain a set of high resolution images for further palaeontological studies. Additionally, this technique can be complemented with other techniques [46] and with other components, like DLPs, to get faster results.

References

1. S. S. Gorthi, and P. Rastogi, “Fringe projection techniques: whither we are?,” Opt. Lasers Eng. **48**(2), 133–140 (2010).

2. S. Ma, C. Quan, R. Zhu, and C. J. Tay, “Investigation of phase error correction for digital sinusoidal phase-shifting fringe projection profilometry,” Opt. Lasers Eng. **50**(8), 1107-1118 (2012).

3. T. M. Kaiser, and H. Katterwe, “The application of 3D-microprofilometry as a tool in the surface diagnosis of fossil and sub-fossil vertebrate hard tissue. An example from the pliocene upper laetolil beds, Tanzania,” Int. J. Osteoarchaeol. **11**, 350–356 (2001).

4. Huang, L., Chua, P.S.K., and Asundi, A. 2010. Least-squares calibration method for fringe projection profilometry considering camera lens distortion. Applied Optics, 49:1539-1548.

5. S. Zhang, and P. S. Huang, “Novel method for structured light system calibration,” Opt. Eng. **45**(8), 083601-083608 (2006).

6. T. Hoang, B. Pan, D. Nguyen, and Z. Wang, “Generic gamma correction for accuracy enhancement in fringe-projection profilometry,” Opt. Lett. **35**, 1992–1994 (2010).

7. Yang, F. and He, X. 2007. Two-step phase-shifting fringe projection profilometry: intensity derivative approach. Applied Optics, 46:7172-7178.

8. M. A. Gdeisat, A. Abid, D. R. Burton, M. J. Lalor, F. Lilley, C. Moore, and M. Qudeisat, “Spatial and temporal carrier fringe pattern demodulation using the one-dimensional continuous wavelet transform: Recent progress, challenges, and suggested developments,” Opt. Lasers Eng. **47**(12), 1348-1361 (2009).

9. Arroyo-Cabrales, J. and Alvarez, T. 1990. Restos óseos de murciélagos procedentes de las excavaciones en las grutas de Loltún. Instituto Nacional de Antropología e Historia, Serie Prehistórica, 194:1-103.

10. Alvarez, T. 1982. Restos de mamíferos recientes y pleistocénicos procedentes de las grutas de Loltún, Yucatán, México. Cuaderno de Trabajo 26. Instituto Nacional de Antropología e Historia, 26:7-35.

11. Gutiérrez-García, T.A., Vázquez-Domínguez, E, Arroyo-Cabrales, J., Kuch, M., Enk, J., King, C., and Poinar, H.N. 2014. Ancient DNA and the Tropics, a rodent’s tale. Biology Letters, 10:20140224.

12. Hofreiter, M., Serre, D., Poinar, H.N., Kuch, M., and Pääbo, S. 2001. Ancient DNA. Nature Reviews Genetics, 2:353-359.

13. Herrmann, B. and Hummel, S. 1994. Ancient DNA, Recovery and Analysis of Genetic Material from Paleontological, Archaeological, Museum, Medical and Forensic Specimens. Springer-Verlag, New York.

14. Pan, B., Kemao, Q., Huang, L., and Asundi, A. 2009. Phase error analysis and compensation for nonsinusoidal waveforms in phase-shifting digital fringe projection profilometry. Optics Letters, 34:416-418.

15. J. C. Gutiérrez-García, J. F. Mosiño, A. Martínez, T. A. Gutiérrez-García, E. Vázquez-Domínguez, and J. Arroyo-Cabrales, "Practical eight-frame algorithms for fringe projection profilometry," Opt. Express **21**, 903-917 (2013).

16. Goodhead, D.T. 1994. Initial events in the cellular effects of ionizing radiations: clustered damage in DNA. International Journal of Radiation Biology, 65:7-17.

17. Risom, L., Moller, P., Vogel, U., Kristjansen, P.E., and Loft, S. 2003. X-ray-induced oxidative stress: DNA damage and gene expression of HO-1, ERCC1 and OGG1 in mouse lung. Free Radical Research, 37:957-966

18. Agrawala, P.K., Eschenbrenner, A., Penhoat, M.A.H.D., Boissiere, A., Politis, M.F., Touati, A., Sage, E. and Chetioui, A. 2008. Induction and repairability of DNA damage caused by ultrasoft X-rays: role of core events. International Journal of Radiation Biology, 84:1093-1103.

19. Parplys, A.C., Petermann, E., Petersen, C., Dikomey, E., and Borgmann, K. 2012. DNA damage by X-rays and their impact on replication processes. Radioterapy and Oncology, 102:466-471.

20. Sansoni, G., Carocci, M., and Rodella, R. 1999. Three-dimensional vision based on a combination of gray-code and phase-shift light projection: analysis and compensation of the systematic errors. Applied Optics, 38:6565-6573.

21. D. Ghiglia and M. D. Pritt, "Two-Dimensional Phase Unwrapping theory, algorithms, and software," John Wiley & Sons, Inc. 1998.

22. Goldstein, R.M., Zebker, H.A., and Werner, C.L. 1988. Satellite radar interferometry: two-dimensional phase unwrapping. Radio Science, 23:713-720.

23. Li, J.L., Su, X.Y., Su, H.J., and Cha, S.S. 1998. Removal of carrier frequency in phase-shifting techniques. Optics and Lasers in Engineering, 30:107-115.

24. Cignoni, P., Corsini, M., and Ranzuglia, G. 2008. MeshLab: an open-soirce 3D mesh processing system. ERCIM News, 73:47-48.

25. Tafforeau, P., Boistel, R., Boller, E., Bravin, A., Brunet, M. Chaimanee, Y., Cloetens, P., Feist, M., Hoszowska, J., Jaeger, J.J., Kay, R.F., Lazzari, V., Marivaux, L., Nel, A., Nemoz, C., Thibault, X., VIgnaud, P., and Zabler, S. 2006. Applications of X-ray synchrotron microtomography for non-destructive 3D studies of paleontological specimens. Applied Physics A, 83:195-202.

26. Sutton, M.D. 2008. Tomographic techniques for the study of exceptionally preserved fossils. Proceedings of the Royal Society B, 275:1587-1593.

27. Abel, R.L., Rettodini, C. and Richter, M. 2012. A palaeobiologist's guide to 'virtual' micro-CT preparation. Palaeontologia Electronica, 15:6T-17p.

28. Sánchez, S., Fernandez, V., Pierce, S.E., Tafforeau, "Homogenization of simple absorption for the imaging of large and dense fossils with synchrotron microtomography," Nature Protocols **8**, 1708-1717 (2013).

29. Cunningham, J.A., Rahman, I.A., Lautenschlager, S., Rayfield, E.J., Donoghue, C.J. 2014. A virtual world of paleontology. Trends in Ecology & Evolution, 29:347-357.

30. Rahman, I.A. and Smith, S.Y. 2014. Virtual Paleontology: computer aided analysis of fossil form and function. Journal of Paleontology, 88:633–635.

31. Sutton, M., Rahman, I. and Garwood, R. 2014. Techniques for Virtual Palaeontology.John Wiley & Sons, England.

32. Thomas, D.B. 2011. Illuminating fossils by NIR. NIR News, 22:6-8.

33. Carré, P. and Hamon, J. 1966. Mesure interférentielle de la base géodésique du Bureau International des poids et mesures. Metrología, 2:143-150.

34. Y. Surrel, "Phase stepping: a new self-calibrating algorithm," Appl. Opt. **32**(19), 3598–3600 (1993).

35. Martínez, A., Rayas, J.A., Cordero, R.R., Balieiro, D., Labbe, F. "Leaf cuticle topography retrieved by using fringe projection," Opt. Lasers Eng. **50**, 231-235 (2012).

36. Conroy, M. and Armstrong, J. 2005. A comparsion of surface metrology techniques. Journal of Physics, 13:458-465.

37. Li, D. and Kofman, J. 2014. Adaptive fringe-pattern projection for image saturation avoidance in 3D surface-shape measurement. Optics Express, 22:9887-9901.

38. Kielbassa, C., Roza, L. and Epe, B. 1997. Wavelenght dependence of oxidative DNA damage induced by UV and visible light. Carcinogenesis, 18:811-816.

39. Solarczyk, K.J., Zarebski, M. and Dobrucki, J.W. 2012. Inducing local DNA damage by visible light to study chromatin repair. DNA Repair, 11:996-1002.

40. Muñoz-Muñoz, F., Perpiñán, D. "Measurement error in morphometric studies: comparison between manual and computerized methods," Annales Zoologici Fennici **47**, 46-56 (2010).

41. Padmapriya, A. and Vigneshnarthi, S. 2012. Image processing operations for 3d image. International Journal of Scientific and Research Publications, 2:1-6.

42. Falkingham, P. L. 2012. Acquisition of high resolution 3D models using free, open-source, photogrammetric software. Palaeontologia Electronica,15:15p.

43. Adams, D.C., Rohlf, F.J., and Slice, D.E. 2004. Geometric morphometrics: ten years of progress following the 'revolution'. Italian Journal of Zoology, 71:5-16.

44. Angielczyk, K.D. and Sheets, H.D. 2007. Investigation of simulated tectonic deformation in fossils using geometric morphometrics. Paleobiology, 33:125–148.

45. P. Carré, “Installation et utilisation du comparateur photoélectrique et interférentiel du bureau international des poids et mesures,” Metrologia **2**, 13–23 (1966).

46. Lopez-Ortiz B., Toto-Arellano N.-I., Flores Muñoz V. H., Martínez García A., García Lechuga L., Martínez Domínguez J.-A. “Phase profile analysis of transparent objects through the use of a two windows interferometer based on a one beam splitter configuration,” Optik, **125**, 7227-7230 (2014).

Chapter 5

General conclusions and remarks

5.1. Conclusions and future work

In this work, four novel filters corresponding to eight-frame algorithms to solve the problem of the reconstruction of three-dimensional surfaces in semi-fossilized materials are presented. They are able to estimate accurately the phase shifts by minimizing the high-order correlations between the reconstructed phases and the reconstructed amplitudes of the reference wave, which are introduced by phase shift errors in PSP. The proposed algorithms are not reported previously, and they were tested experimentally besides by simulations. Additionally, they were compared with traditional eight step PSP methods. In particular, the MBE filter reduces significantly the influence of the bias error and harmonics. This algorithm has several advantages over similar. First, it allows to analyze materials with several optical properties involved in miscalibrations and phase errors. Second, it is suitable for studies that involve FPP systems. The effectiveness and improvement of the proposed algorithms and procedures have been supported and confirmed by our simulations and experimental results. With this new algorithms, we were able to fulfil the main aim of this work, to develop a robust and reliable algorithm for optical techniques as the FPP, and that can be applied to obtain 3D images of semi-fossils (and other biological objects), preserving at the same time key biological and detailed morphological information.

With the results obtained in this thesis, a new path is opened for the use of custom filters designed for specific experiments, and this simply that with more information of the samples without sacrificing high costs in material and computational power. It has a vast potential application for ancient DNA and fossil studies where small –to extremely small as in our case– samples are involved that need to be destroyed for DNA extraction and molecular analysis. Finally, the images obtained with this technique can be used in a wide variety of studies, like comparing the anatomical features of extant and extinct organisms based on geometric

morphometrics or to evaluate the tectonic deformation in fossils. Furthermore, this work will have a direct repercussion in biologic and palaeontologic institutions responsible of the preservation of palaeontological, anthropological and historical heritage. The information obtained by using this new optical techniques and algorithms will permit the posteriori phylogenetics specie's identification and classification.

5.2 List of publications

1. J. F. Mosiño, ***J. C. Gutiérrez-García***, T. A. Gutiérrez-García, and J. M. Macías-Preza, "Two-frame algorithm to design quadrature filters in phase shifting interferometry," Opt. Express **18**, 24405-24411 (2010).

2. J. F. Mosiño, ***J. C. Gutiérrez-García***, T. A. Gutiérrez-García, F. Castillo, M. A. García-González, and V. A. Gutiérrez-García, "Algorithm for phase extraction from a set of interferograms with arbitrary phase shifts," Opt. Express **19**, 4908-4923 (2011).

3. ***Juan C. Gutiérrez-García***, J. F. Mosiño, Amalia Martínez, Tania A. Gutiérrez-García, Ella Vázquez-Domínguez, and Joaquín Arroyo-Cabrales, "Practical eight-frame algorithms for fringe projection profilometry," Opt. Express **21**, 903-917 (2013).

4. ***Juan C. Gutiérrez-García***, Tania A. Gutiérrez-García, Juan F. Mosiño, Ella Vázquez-Domínguez, Amalia Martínez-García, Joaquín Arroyo-Cabrales, "A novel application of the white light/fringe projection duo: recovering high precision 3D images from fossils for the digital preservation of morphology", Palaeontologia Electronica **18.2.6T**, 1-13 (2015).

5. ***J.C. Gutiérrez-García,*** J.F. Mosiño, Amalia Martínez, "Tunable eight-frame filters with arbitrary steps for temporal phase shifting", Optik (2015).

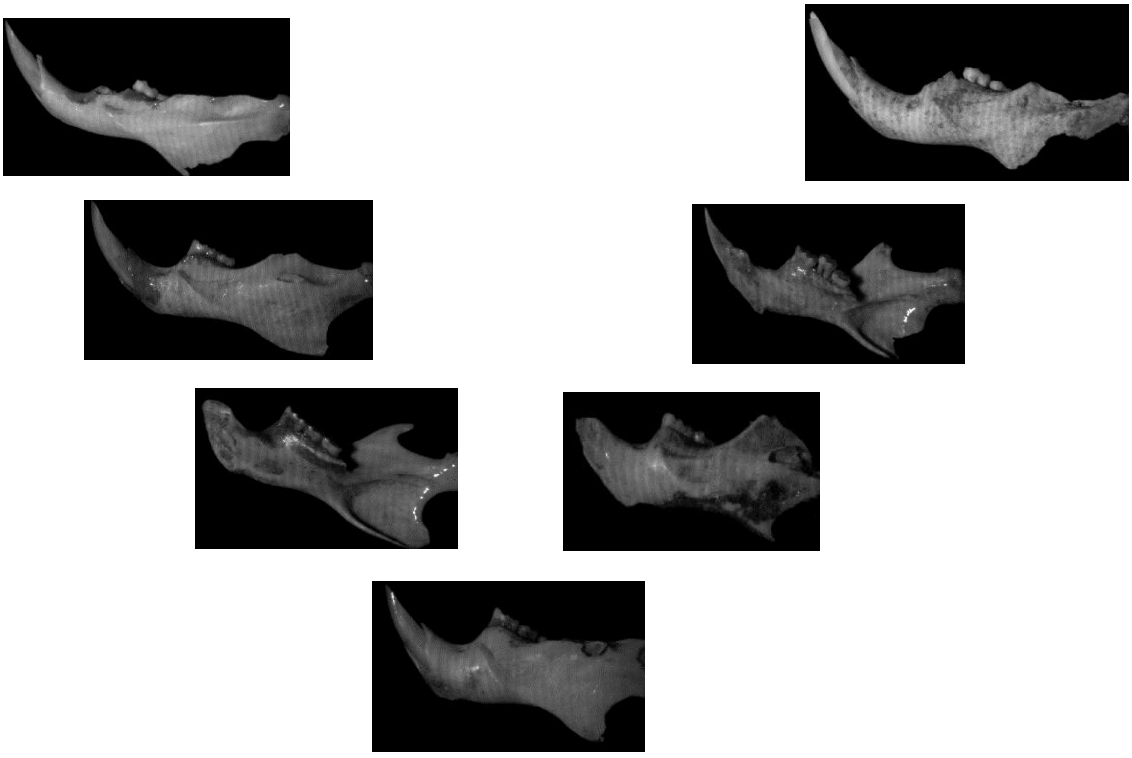

End